

CHEMICAL ENRICHMENT OF DAMPED LYMAN ALPHA SYSTEMS AS A DIRECT CONSTRAINT ON POPULATION III STAR FORMATION

GIRISH KULKARNI¹, EMMANUEL ROLLINDE², JOSEPH F. HENNAWI¹, ELISABETH VANGIONI²

Draft version March 6, 2018

ABSTRACT

Observations of damped Ly α absorbers (DLAs) can be used to measure gas-phase metallicities at large cosmological lookback times with high precision. Furthermore, relative abundances can still be measured accurately deep into the reionization epoch ($z > 6$) using transitions redward of Ly α , even though Gunn-Peterson absorption precludes measurement of neutral hydrogen. In this paper we study the chemical evolution of DLAs using a model for the coupled evolution of galaxies and the intergalactic medium (IGM), which is constrained by a variety of observations. Our goal is to explore the influence of Population III stars on the abundance patterns of DLAs to determine the degree to which abundance measurements can discriminate between different Population III stellar initial mass functions (IMFs). We include effects such as inflows onto galaxies due to cosmological accretion and outflows from galaxies due to supernova feedback. A distinct feature of our model is that it self-consistently calculates the effect of Population III star formation on the reionization of an inhomogeneous IGM, thus allowing us to calculate the thermal evolution of the IGM and implement photoionization feedback on low-mass galaxy formation. We find that if the critical metallicity of Population III to II/I transition is $\lesssim 10^{-4} Z_{\odot}$, then the cosmic Population III star formation rate (SFR) drops to zero for $z < 8$. Nevertheless, at high redshift ($z \sim 6$) chemical signatures of Population III stars remain in low mass galaxies (halo mass $\lesssim 10^9 M_{\odot}$). This is because photoionization feedback suppresses star formation in these galaxies until relatively low redshift ($z \sim 10$), and the chemical record of their initial generation of Population III stars is retained. We model DLAs as these low-mass galaxies, and assign to them a mass-dependent H I absorption cross-section in order to predict the expected distribution of DLA abundance ratios. We find that these distributions are anchored towards abundance ratios set by Population II supernovae yields, but they exhibit a tail which depends significantly on the Population III IMF for $z > 5$. Thus, a sample of DLA metallicity and relative abundance measurements at high-redshift holds the promise to constrain Population III enrichment and the Population III IMF. We find that sample of just 10 DLAs with relative abundances measured to an accuracy of 0.1 dex is sufficient to constrain the Population III IMF at 4σ . These constraints may prove stronger than other probes of Population III enrichment, such as metal-poor stars and individual metal-poor DLAs. Our results provide a global picture of the thermal, ionization, and chemical evolution of the Universe, and have the potential to rule out certain Population III scenarios.

Subject headings: cosmology: dark ages, reionization, first stars – galaxies: abundances – galaxies: evolution – galaxies: ISM – galaxies: quasars: absorption lines – stars: Population III

1. INTRODUCTION

The first stars in the Universe formed out of the primordial interstellar media (ISM) of the first galaxies and are therefore expected to be metal-free. Formation of these so-called Population III stars is an important milestone in cosmic evolution as the UV photons produced by these objects presumably initiated the process of reionization of the intergalactic medium (IGM). Reionization, and the consequent reheating of the IGM result in new physical processes, such as photoionization feedback, that are expected to influence subsequent galaxy formation and evolution. Apart from reionization, Population III stars are also expected to contribute to chemical feedback. The metal yield of these stars can pollute the ISM to create conditions for formation of metal-enriched Population II stars that we observe today. Population III

stars have also been invoked to seed the formation of supermassive black holes seen in centres of galaxies at low redshift. In the Λ CDM universe, in which galaxies begin their evolution with primordial abundances, Population III must have formed at some point. Still, their observational signatures and evidence for their existence is still elusive. (The only hints so far are from extremely metal-poor stars in the Milky Way's halo, as we describe below.) These stars thus form a significant piece of the puzzle of galaxy formation (Bromm & Larson 2004; Loeb 2010).

The initial conditions of galaxy formation are well known thanks to cosmological constraints at the last scattering surface (Ciardi & Ferrara 2005; Bromm & Yoshida 2011). In the first galaxies that result from these initial conditions (at $z \gtrsim 20$ in dark matter haloes with mass of about $10^6 M_{\odot}$), gas can fragment to form Population III stars. The chemistry of gas in these haloes is simple, and formation of the first generation of stars is unaffected by complicated effects like

¹ Max Planck Institute for Astronomy, Königstuhl 17, 69117 Heidelberg, Germany; girish@mpia-hd.mpg.de

² Institut d'Astrophysique de Paris, UMR 7095, UPMC, Paris VI, 98 bis boulevard Arago, 75014 Paris, France

feedback. Physical factors such as magnetic fields are expected to play a negligible role in the formation of Population III stars as dynamically significant magnetic fields are not expected to be present in Population III star-forming clouds (Bromm & Larson 2004; Turk et al. 2012). We can therefore hope that the physics of Population III star formation is simpler than that of star formation in the present day universe.

Nonetheless, properties of Population III stars, such as their mass, are not well-understood. This is primarily because of the wide range of scales involved in the fragmentation and collapse of gas in high redshift haloes. On the galactic scale, the mass of the first galaxies is debatable (Bromm & Yoshida 2011). Since the molecular hydrogen cooling threshold provides a lower bound on halo mass for gas cooling and fragmentation, we expect that the first stars will be hosted by haloes with virial temperature $T_{\text{vir}} = 10^3$ K. However, molecular hydrogen is fragile and can be easily destroyed as the IGM is transparent at the required energies. If the molecular hydrogen is destroyed by the Lyman-Werner background produced by the very first few stars, then the formation of new stars could be delayed up to a lower redshift in all but the most massive haloes (e.g., Barkana & Loeb 2001). On the proto-stellar scale, it is unclear whether the gas collected in these haloes will fragment, or what will be the mass of the fragments if it does. It has been suggested that dynamical effects can cause fragmentation even when metal-line cooling is not available (Dopcke et al. 2012). But the magneto-hydrodynamics in this regime is very difficult to simulate. In summary, both the initial mass function (IMF) as well as the cosmic star formation rate (SFR) history of Population III stars remain unclear. We are thus forced to ask if there are any empirical constraints on these quantities.

Unfortunately, no understanding of Population III stars has emerged from the observational side either. Currently, two lines of observational inquiry have aimed at an unambiguous detection of the chemical signatures of Population III stars. These probe either (1) low-mass extremely metal-poor stars in the Galaxy’s halo, or (2) metal-poor neutral gas reservoirs, presumably galaxies, seen in quasar absorption spectra at high redshift ($z \gtrsim 2$) as damped Ly α absorbers (DLAs). In the first case, Galactic stellar archaeology has been considered as an important probe of high redshift star formation environment (Frebel 2011). These long-lived stars could potentially carry signatures of enrichment by Population III supernovae (Rollinde et al. 2009; Spite et al. 2013). However, no detection of a truly metal-free star has been made to date. The lowest-metallicity star known has $[\text{Fe}/\text{H}] = -4.88 \pm 0.12$ (Caffau et al. 2011), although current observations have a potential sensitivity of metallicity down to $[\text{Fe}/\text{H}] = -9.8$ (Frebel & Norris 2011). Moreover, although they are a valuable tool for constraining Galactic chemical evolution, it is not clear if metal-poor stars are an unambiguous probe of the cosmic SFR and IMF of Population III stars, because these observations are limited to the peculiar star formation and assembly history of the Galaxy and because abundance ratios in a single metal-poor star cannot probe the whole Population III IMF. In the second case, metal-poor DLAs at $z \sim 2$ likely represent systems that form in peculiar, pristine patches of the IGM. They could be direct

descendants of high redshift haloes and, due to inefficient star formation, probably retain signature of Population III star formation (Salvadori & Ferrara 2009, 2012). However, observations of such systems have also failed to show up chemical abundance patterns that cannot be explained with Population II yields (Matteucci & Calura 2005; Cooke et al. 2011; Fumagalli et al. 2012).

In the absence of current observational constraints, there are suggestions that future facilities such as the James Webb Space Telescope (JWST) and the Large Synoptic Survey Telescope (LSST) may detect pair-instability supernovae (PISN) from any high-mass Population III stars in situ at high redshift (Pan et al. 2012a,b). It has also been argued that massive Population III stars could trigger long GRBs (Bromm & Loeb 2006). Detection of these objects will also potentially probe the first stars (Levesque 2012).

In this paper, we study the possibility of probing the Population III SFR and IMF by measuring chemical abundance ratios in low mass galaxies at high redshift ($z \sim 6$). We set up a conservative model of evolution of galaxies and the IGM, constrained by low-redshift observations, and show that different Population III IMFs leave distinct signatures in the metal abundance ratios of low mass galaxies at high redshift. Further, these galaxies can be observed as DLAs in the spectra of any background quasars. These absorption-line observations can be used to measure gas-phase metallicities in these galaxies with high precision. Even deep into the reionization epoch ($z > 6$), abundance ratios can still be measured accurately in such systems using transitions redward of Ly α . We model DLAs as these low-mass galaxies by assigning them a mass-dependent H I absorption cross section, and predict the expected distribution of DLA abundance ratios at various redshifts. We find that at high redshift *the distribution of DLAs in the abundance-ratio space can be mapped to a combination of Population III SFR and IMF*. This can be a powerful probe of the first stars.

We describe our modeling of the evolution of galaxies and the IGM in Section 2. Our results are presented in Section 3. We discuss some caveats in Section 4 and present a summary of conclusions in Section 5. Throughout this paper, we assume a WMAP 9-yr cosmology (Hinshaw et al. 2012).

2. MODELING GALAXY AND IGM EVOLUTION

Given a dark matter halo of mass M_h at $z = 0$, we can calculate its complete *mean* assembly history. This can be done using the extended Press-Schechter formalism, or using large volume N-body simulations of structure formation. We prefer the latter approach for its accuracy, and use fitting functions provided by Fakhouri et al. (2010). This lets us calculate the mean dark matter mass M of a halo at any stage of its assembly history. We use this to set up a model of baryonic evolution inside the halo. In simplest terms, this model assumes that a halo (1) accretes baryons through cosmological accretion, (2) forms stars from any gas contained in the halo for sufficiently long duration, and (3) ejects baryons due to supernova-induced outflows.

With these assumptions, we can associate with each dark matter halo a stellar mass M_* and a gas mass M_g at any point in its assembly history. Further, using stel-

lar population synthesis, we can also calculate the total amount of metals M_Z and the rate of UV photon production \dot{n}_{ph} in a halo at any stage of its assembly history. All of these quantities are functions of the redshift-zero halo mass (M_h). We repeat this exercise for a number of logarithmically spaced halo masses between M_h^{low} and M_h^{high} , two values that are chosen using a convergence criterion. The integrated UV photon yield of all halos in this mass range is then used in a reionization model to calculate the ionization and thermal history of the IGM. Similarly, the integrated outflow yield is used with a chemical enrichment model to calculate the average IGM metallicity. The IGM ionization, thermal, and chemical evolution models feed back into the galaxy formation model through photoionization feedback, which controls the thermal cut-off on the mass of star-forming haloes, and by changing the metallicity of inflows from the IGM to the galaxies.

This galaxy formation picture is often referred to as the “bathtub” model, and has been used to study various problems in galaxy formation to a reasonable degree of accuracy (Bouché et al. 2010; Krumholz & Dekel 2012). We will now describe our method in detail. A summary of free parameters of our model is presented in Table 2.

2.1. Halo growth

The mean mass growth rate of dark matter haloes in the Λ CDM cosmology can be parameterised by the fitting function (Fakhouri et al. 2010)

$$\dot{M}(z) = 46.1 \frac{M_\odot}{\text{yr}} (1 + 1.1z) \times \sqrt{\Omega_m(1+z)^3 + \Omega_\Lambda} \left(\frac{M(z)}{10^{12} M_\odot} \right)^{1.1}, \quad (1)$$

where $M(z)$ denotes the mean mass in the main branch of the merger tree of a halo at redshift z . This growth rate corresponds to the mean rate of growth of halo mass. This relation can be understood in terms of the extended Press-Schechter picture of structure formation (Neistein & Dekel 2008). By comparing it with cosmological simulations, Fakhouri et al. (2010) have shown that it is accurate over a mass range spanning at least five orders of magnitude ($10^{10} M_\odot$ to $10^{15} M_\odot$ at $z = 0$) and a wide range of redshifts ($0 \leq z \lesssim 15$). Integrating Equation (1) with the boundary condition $M(z = 0) = M_h$ gives the mean mass of a halo at any redshift. Note that this describes the evolution of the dark matter mass of the halo.

2.2. Baryons

Baryonic content of galaxies is influenced by gas inflows, gas outflows, and star formation. Hydrodynamical simulations suggest that these processes tend to be in equilibrium (Davé et al. 2012). We now describe these processes and calculate the mean evolution of gas mass (M_g), stellar mass (M_*), and metal mass (M_Z) in each halo mass bin. The metal mass term describes the mass of the metals in the gas phase (ISM); it excludes the metals that are locked up inside stars.

2.2.1. Gas

Gas inflows replenish the gas content of haloes as they evolve. We assume that the mean gas inflow rate is proportional to the mean halo growth rate

$$\dot{M}_{g,\text{in}}(z) = f_{g,\text{in}} \left(\frac{\Omega_b}{\Omega_m} \right) \dot{M}(z). \quad (2)$$

We follow Bouché et al. (2010) and take the constant of proportionality to be $f_{g,\text{in}} = 0.7$, except when the halo mass is below the filtering mass M_{min} (described below), in which case there is no gas inflow and we set $f_{g,\text{in}} = 0$. The choice of these values is motivated by the comparison of measured SFR in massive high-redshift galaxies with predicted gas accretion rates (Genel et al. 2008; Dekel et al. 2009; Bauermeister et al. 2010).

Once inside the halo, some of the accreted gas is lost to star formation. The amount of gas lost is

$$\dot{M}_{g,\text{sf}}(z) = -\psi(z) + \int_{m_l}^{m_u} dm \phi(m) \cdot \psi[t(z) - \tau(m)] \cdot [m - m_r(m)], \quad (3)$$

where the ψ is the star formation rate (which we describe below), and the second term accounts for mass loss from evolving stars via stellar winds and supernova explosions. In the second term, $\phi(m)$ is the stellar IMF, $m_r(m)$ is the remnant mass left by a star with initial mass m , $\tau(m)$ is its lifetime, and $t(z)$ is the cosmic time. The lower limit m_l of the integral is such that $\tau(m_l) = t(z)$. (The upper limit m_u corresponds to the high-mass limit of the stellar IMF, which we discuss below.) The instantaneous recycling approximation (IRA) is often used in calculating the mass loss from stars (e.g., Krumholz & Dekel 2012). In this approximation, stars with initial mass above a certain value m_0 are assumed to die instantaneously ($\tau = 0$) while those with initial mass less than m_0 are assumed to live forever ($\tau = \infty$). However, although this is a reasonable assumption to make while studying, say, the solar neighbourhood, it is not a good approximation at high redshift, when stellar lifetimes are comparable to the Hubble time. Therefore, we do *not* use IRA in Equation (3).

Gas is also lost due to outflows resulting out of supernova-driven winds. This effect is expected to be proportional to the star formation rate and inversely proportional to the depth of the halo potential well (Daigne et al. 2006; Erb 2008; Bouché et al. 2010; Krumholz & Dekel 2012). We write the mass loss due to outflows as

$$\dot{M}_{g,\text{out}}(z) = -\frac{2\epsilon}{v_{\text{esc}}^2} \int_{m_l}^{m_u} dm \{ \phi(m) \times \psi[t(z) - \tau(m)] \cdot E_{\text{kin}}(m) \}, \quad (4)$$

where $v_{\text{esc}}^2 = 2GM/R_{\text{vir}}$ is the escape velocity of the halo, and $E_{\text{kin}}(m)$ is the kinetic energy released by a star of mass m . The parameter ϵ is fixed by calculating the total baryon fraction in structures, $f_{b,\text{struct}}$, at $z = 0$ (Fukugita & Peebles 2004).

Combining the contribution of above three processes of star formation, inflows, and outflows, the evolution of the gas mass of a halo can be written as

$$\dot{M}_g(z) = \dot{M}_{g,\text{in}}(z) + \dot{M}_{g,\text{sf}}(z) + \dot{M}_{g,\text{out}}(z), \quad (5)$$

where each term is redshift- and halo-mass-dependent.

2.2.2. Stars

We assume that the star formation rate, ψ , in a halo tracks the total amount of cold gas, M_{cool} , inside that halo. Thus

$$\psi = f_* \left(\frac{M_{\text{cool}}}{t_{\text{dyn}}} \right), \quad (6)$$

where t_{dyn} is the halo dynamical time and f_* is a free parameter. The cold gas mass is calculated by defining a local cooling rate within the halo,

$$t_{\text{cool}}(r) = \frac{3k_B T \rho_g(r)}{2\mu n_H^2(r) \Lambda(T)}, \quad (7)$$

where ρ_g is the (spherically symmetric) gas density profile, n_H is the hydrogen number density, μ is the molecular weight and Λ is the cooling function. A cooling radius r_{cool} can then be defined by

$$t_{\text{cool}}(r_{\text{cool}}) = t_{\text{dyn}}, \quad (8)$$

which gives the cooling rate as

$$\frac{dM_{\text{cool}}}{dt} = 4\pi \rho_g(r_{\text{cool}}) r_{\text{cool}}^2 \frac{dr_{\text{cool}}}{dt}. \quad (9)$$

Initially all gas entering the halo is shock-heated to the virial temperature. Integrating Equation (9) then gives the amount of cool gas at any time. We use a gas profile close to isothermal, which fits the results of [Springel & Hernquist \(2003\)](#) to better than 10%. Equation (6) follows from the empirical Kennicutt-Schmidt (KS) relation ([Krumholz & Thompson 2007](#)) in the limit of marginally unstable disks. The KS relation does not exhibit any evolution till $z \sim 2$ ([Daddi et al. 2010](#)).

The galaxy dynamical time can be written as

$$t_{\text{dyn}} = 2 \times 10^7 \text{ yr} \left(\frac{R_{1/2}}{4 \text{ kpc}} \right) \left(\frac{V_c}{200 \text{ km s}^{-1}} \right)^{-1}, \quad (10)$$

where $R_{1/2}$ is galaxy disk scale-length and V_c is the halo circular velocity ([Bouché et al. 2010](#)). We take the disk scale-length to be proportional to the halo virial radius

$$R_{1/2} = 0.05 \left(\frac{\lambda}{0.1} \right) R_{\text{vir}}, \quad (11)$$

where the halo spin parameter λ is taken to be 0.07 ([Krumholz & Dekel 2012](#)). The halo circular velocity is given by

$$V_c = 23.4 \left(\frac{M}{10^8 h^{-1} M_\odot} \right)^{1/3} \left[\frac{\Omega_m}{\Omega_m^z} \frac{\Delta_c}{18\pi^2} \right]^{1/6} \times \left(\frac{1+z}{10} \right)^{1/2} \text{ km/s}, \quad (12)$$

where

$$\Omega_m^z = \frac{\Omega_m(1+z)^3}{\Omega_m(1+z)^3 + \Omega_\Lambda + \Omega_k(1+z)^2}, \quad (13)$$

and Δ_c is the halo overdensity relative to the cosmological critical density, given by

$$\Delta_c = 18\pi^2 + 82d - 39d^2, \quad (14)$$

for the Λ CDM cosmology, where $d = \Omega_m^z - 1$ ([Barkana & Loeb 2001](#)). The virial radius is given by

$$R_{\text{vir}} = 0.784 \left(\frac{M}{10^8 h^{-1} M_\odot} \right)^{1/3} \left[\frac{\Omega_m}{\Omega_m^z} \frac{\Delta_c}{18\pi^2} \right]^{-1/3} \times \left(\frac{1+z}{10} \right)^{-1} h^{-1} \text{ kpc}. \quad (15)$$

The total stellar mass in the halo evolves as

$$\dot{M}_*(z) = -\dot{M}_{g,\text{sf}}(z) = \psi(z) - \int_{m_l}^{m_u} dm \phi(m) \cdot \psi[t(z) - \tau(m)] \cdot [m - m_r(m)], \quad (16)$$

where, as in Equation (3), the second term on the right hand side accounts for mass loss from stars.

2.2.3. Metals

The initial mass of metals in a halo is zero. Metals are produced in stars in the halo and are mixed in the halo gas when stars explode as supernovae, and due to stellar winds. The total mass of metals M_Z in the halo is also affected by inflows from the IGM and outflows into it. The inflow term is given by

$$\dot{M}_{Z,\text{in}}(z) = Z_{\text{IGM}}(z) \dot{M}_{g,\text{in}}, \quad (17)$$

where Z_{IGM} is the metal abundance in the IGM, which we describe below.

Metal outflows can be described in similar fashion, as

$$\dot{M}_{Z,\text{out}}(z) = -Z_g(z) \dot{M}_{g,\text{out}}, \quad (18)$$

where $Z_g \equiv M_Z/M_g$ is the gas metal abundance in the halo.

Lastly, the effect of star formation can be expressed as ([Krumholz & Dekel 2012](#))

$$\dot{M}_{Z,\text{sf}}(z) = \int_{m_l}^{m_u} dm \phi(m) \cdot \psi[t(z) - \tau(m)] \times mp_Z(m)(1 - \zeta). \quad (19)$$

Here, $p_Z(m)$ is the mass fraction of a star of initial mass m that is converted to metals and ejected. The factor $1 - \zeta$ takes into account the fact that not all of the newly enriched material is going to mix in the ISM. Some of it will be directly ejected out of the halo due to supernova explosions. We follow [Krumholz & Dekel \(2012\)](#) and write

$$\zeta = \zeta_l \exp(-M_{h,12}/M_{\text{ret}}), \quad (20)$$

where $M_{h,12}$ is the halo mass in units of $10^{12} M_\odot$ and we set the parameters $M_{\text{ret}} = 0.3$ and $\zeta_l = 0.9$. These values are expected to depend on the stellar IMF and the problem geometry. Our choice of these values is motivated by the simulations of [Mac Low & Ferrara \(1999\)](#) and the findings of [Krumholz & Dekel \(2012\)](#). These authors find that changing these quantities within reasonable limits has only a modest effect on the star formation and metallicity evolution.

The evolution of the metal mass of a halo can now be written as

$$\dot{M}_Z(z) = \dot{M}_{Z,\text{sf}}(z) + \dot{M}_{Z,\text{out}}(z) + \dot{M}_{Z,\text{in}}(z). \quad (21)$$

Table 1
Stellar IMFs used in this paper

Model	Pop. III IMF	Pop. II IMF
Model 1	1–100 M_{\odot} Salpeter	0.1–100 M_{\odot} Salpeter
Model 2	35–100 M_{\odot} Salpeter	0.1–100 M_{\odot} Salpeter
Model 3	100–260 M_{\odot} Salpeter	0.1–100 M_{\odot} Salpeter

2.3. IMF

We always take the stellar IMF to have the Salpeter form, which is given by

$$\phi(m) = \phi_0 m^{-2.3}, \quad (22)$$

where the constant ϕ_0 is chosen such that

$$\int_{m_0}^{m_1} dm m \phi(m) = 1 M_{\odot}. \quad (23)$$

We take $m_0 = 0.1 M_{\odot}$ and $m_1 = 100 M_{\odot}$ for Population I/II stars. Population III stars have different IMF in each of our models, as we want to discuss the effect of Population III IMF on various quantities. These are shown in Table 1. The stellar IMF in model 3 covers the pair instability supernova range, whereas models 1 and 2 explore the effect of AGB stars and core collapse supernovae respectively. Each model is calibrated separately to reproduce the cosmic star formation rate (SFR) history, the IGM Thomson scattering optical depth to the last scattering surface ($\tau_e = 0.089 \pm 0.014$ Hinshaw et al. 2012), and the hydrogen photoionization rate in the IGM as measured from Ly α forest observations.

Our model requires stellar lifetimes because we do not assume instantaneous recycling. We take lifetimes for low and intermediate mass stars ($0.1 M_{\odot} < M < 100 M_{\odot}$) from Maeder & Meynet (1989). Lifetimes for stars with higher mass (all of which are Population III) are taken from Schaerer (2002). The model also requires chemical and UV photon yields of stars with different IMFs. Woosley & Weaver (1995) have calculated the chemical yields of massive stars ($12 M_{\odot} < M < 40 M_{\odot}$) with different metallicities ($Z = 0, 10^{-4}, 0.01, 0.1,$ and 1 times solar). We use their results by interpolating between different metallicities and extrapolating beyond the mass range for lower and higher stellar masses. Chemical yields of Population III stars (which are metal-free and high mass) are taken from the calculations of Heger & Woosley (2002). Stellar spectra of Population I/II stars are calculated using STARBURST99 (Leitherer et al. 1999; Vázquez & Leitherer 2005) with respective metallicities. Synthetic spectra of Population III stars are taken from Schaerer (2002).

The transition from Population III star formation to Population II star formation in any halo is implemented via a critical metallicity, Z_{crit} , with our fiducial value as $Z_{\text{crit}} = 10^{-4}$ (Bromm et al. 2001; Bromm & Loeb 2003; Frebel et al. 2007). When the ISM metallicity in a halo crosses Z_{crit} , new stars are formed according to a Population II IMF. We consider the effect of changing the value of Z_{crit} below.

Note that in the chemical evolution model described above, we have only accounted for core-collapse supernovae; the contribution of Type Ia supernovae has been ignored. As implicitly assumed in Equation 19, the core

collapse supernova rate traces star formation activity. The Type Ia supernova rate has a more complex dependence on the stellar IMF and star formation rate.

Classically, progenitors of SNe Ia are thought to be intermediate-mass stars. An unknown delay is expected between the death of the progenitor star and the SN Ia explosion. By using a similar model of cosmic star formation as that presented here, Daigne et al. (2006) argued that the observed rate of SNe Ia occurrence suggests that the typical delay time is long ($\sim 3\text{--}3.5$ Gyr). Using a different model, ? reached a similar conclusion, arguing that observations favour long delay times (~ 1 Gyr). This is also in agreement with recent DLA enrichment measurements at $z = 4\text{--}5$ by Rafelski et al. (2012), who report α -enhancement of about 0.3 in these objects, suggesting that these objects have not yet been enriched by SNe Ia. (As we will discuss below in Section 4, the effect of dust depletion is expected to be low in these systems due to their low metallicity.) If the SNe Ia delay times are indeed sufficiently long, the results of this paper will not be affected, as we are interested in DLA abundances at the highest redshifts ($z \gtrsim 4$).

However, ? have argued that the observed dependence of SNe Ia rate on the colours of parent galaxies, and observed SNe Ia rates in radio-loud early-type galaxies favour a bimodal delay time distribution, in which about half of SNe Ia explode soon after the birth of their progenitor star (short delay time of ~ 100 Myr), while the remaining half have long delay time of the order of 3 Gyr. In the context of DLAs, ? have also shown that when dust depletion is taken into account, most of the claimed DLA α -enhancements vanish, which suggests a role of SNe Ia (cf. ?). While dust is not expected to play a major role in $z \sim 5$ DLAs, these prompt SNe Ia with short delay times can have an effect on the results of our model. Nevertheless, in this paper, we focus on the effect of Population III star formation on the abundance ratios in this paper. We will consider the effects of dust depletion and prompt SNe Ia in a future work (Kulkarni et al. 2013, in preparation). We conjecture here, however, that while such prompt SNe Ia will affect our results, a strong degeneracy with the effect of Population III IMF is unlikely as the latter leave a sufficiently large signature in ratios between α -element abundances ($\sim 0.5\text{--}1$ dex at $z \sim 6$).

2.4. IGM metallicity

Cosmological inflows bring material from the IGM into the ISM of galaxies. The extent to which this dilutes the metal content of the ISM depends on the metallicity of the IGM. We follow the model of Daigne et al. (2006) to calculate the average IGM metallicity at any redshift. This model divides cosmic baryons into three reservoirs: (1) intergalactic medium (subscript ‘‘IGM’’), (2) interstellar medium (‘‘ISM’’), and (3) stars (‘‘str’’). We denote the mass densities of these as M_{IGM} , M_{ISM} and M_{str} respectively. Note that M_{ISM} and M_{str} are mass function weighted integrals of M_g and M_* defined for each halo mass bin above.

The IGM mass density evolves according to

$$\frac{dM_{\text{IGM}}}{dt} = -a_b(t) + o(t), \quad (24)$$

where a_b is the *total* rate of accretion of baryons from

the IGM on to halos of all masses, and $o(t)$ is the total rate of outflow of baryons from halos into the IGM. The stellar mass density evolves as

$$\frac{dM_{\text{str}}}{dt} = \Psi(t) - e(t), \quad (25)$$

where Ψ is the total cosmic star formation rate, and e is rate of ejection of material of stars into the ISM via winds and supernovae, which depends on the stellar IMF. The total cosmic star formation rate is given by

$$\Psi(t) = \int_{M_h^{\text{low}}}^{M_h^{\text{high}}} dM \dot{M}_*(M, t) N(M, t), \quad (26)$$

where M_h^{high} and M_h^{low} are the halo mass limits considered in our calculation (as discussed above), $\dot{M}_*(M, t)$ is star formation rate within a halo of mass M at cosmic time t (given by Equation 16), and $N(M, t)$ is the halo mass function. Lastly, the ISM mass density evolves as

$$\frac{dM_{\text{ISM}}}{dt} = -\frac{dM_{\text{IGM}}}{dt} - \frac{dM_{\text{str}}}{dt}. \quad (27)$$

To calculate the IGM metallicity, in addition to the total masses, the mass fraction of individual elements in each reservoir is also evolved. For an element i , the mass fraction in the IGM is $X_i^{\text{IGM}} = M_i^{\text{IGM}}/M_{\text{IGM}}$ and that in the ISM is $X_i^{\text{ISM}} = M_i^{\text{ISM}}/M_{\text{ISM}}$. It can then be shown that mass fractions in the IGM evolve as

$$\frac{dX_i^{\text{IGM}}}{dt} = o(X_i^{\text{ISM}} - X_i^{\text{IGM}})/M_{\text{IGM}}, \quad (28)$$

and those in the ISM evolve as

$$\begin{aligned} \frac{dX_i^{\text{ISM}}}{dt} = & [a_b(X_i^{\text{IGM}} - X_i^{\text{ISM}}) \\ & + (e_i - eX_i^{\text{ISM}})]/M_{\text{ISM}}. \end{aligned} \quad (29)$$

Here, o is the outflow rate from the ISM and e_i is the rate at which metal i is ejected by stars. In order to completely specify the model, all that is left to specify is (1) initial conditions for above equations, and (2) method of calculation for the three quantities o , a_b , and e .

The total baryon accretion rate is given by

$$\begin{aligned} a_b(t) = & \Omega_b \left(\frac{3H_0^2}{8\pi G} \right) \left(\frac{dt}{dz} \right)^{-1} \left| \frac{df_{\text{struct}}}{dz} \right| \\ = & 1.2h^3 M_{\odot} \text{yr}^{-1} \text{Mpc}^{-3} \left(\frac{\Omega_b}{0.044} \right) \\ & \times (1+z) \sqrt{\Omega_{\Lambda} + \Omega_m(1+z)^3} \left| \frac{df_{\text{struct}}}{dz} \right|, \end{aligned} \quad (30)$$

where f_{struct} is the fraction of total mass in star forming halos. It is given by

$$f_{\text{struct}}(z) = \frac{\int_{M_{\text{min}}}^{\infty} dM M f_{\text{PS}}(M, z)}{\int_0^{\infty} dM M f_{\text{PS}}(M, z)}, \quad (31)$$

and f_{PS} is the Press-Schechter mass function.

Outflows from the ISM into the IGM are described

using the following relation

$$o(t) = \frac{2\epsilon}{v_{\text{esc}}^2(z)} \int_{m_l}^{m_u} dm \phi(m) \cdot \Psi[t(z) - \tau(m)] \cdot E_{\text{kin}}(m), \quad (32)$$

where, as before, ϕ is the stellar IMF, and E_{kin} is the kinetic energy released by the explosion of a star of mass m . The quantity v_{esc} is the ‘‘escape velocity,’’ which is calculated according to

$$v_{\text{esc}}^2(z) = \frac{\int_{M_{\text{min}}}^{\infty} dM f_{\text{PS}}(M, z) M (2GM/R_{\text{vir}})}{\int_{M_{\text{min}}}^{\infty} dM f_{\text{PS}}(M, z) M}. \quad (33)$$

The ejection of enriched gas from stars into the ISM is given by

$$e(t) = \int_{m_l}^{m_u} dm \phi(m) \cdot \Psi[t(z) - \tau(m)] \cdot [m - m_r(m)], \quad (34)$$

as above, where m_u is the upper limit on mass of stars that explode and produce supernova remnants, and m_r is the remnant mass.

2.5. Ionization and thermal evolution of the inhomogeneous IGM

Our model for reionization and thermal history of the average IGM is essentially that developed by Choudhury & Ferrara (2005), with the main difference being in implementation of sources. In this model, which matches a wide range of observational constraints, the IGM is gradually reionized and reheated by star-forming galaxies between $z \sim 20$ and $z \sim 6$. We summarise the main elements of the model here and refer the reader to that paper for details.

The model accounts for IGM inhomogeneities by adopting a lognormal density distribution with the evolution of volume filling factor of ionised hydrogen (H II) regions $Q_{\text{HII}}(z)$ being calculated according to the method outlined by Miralda-Escudé et al. (2000). The volume filling factor of H II regions evolves as

$$\frac{d[Q_{\text{HII}} F_M(\Delta)]}{dt} = \frac{\dot{n}_{\nu}}{n_H} - Q_{\text{HII}} \alpha_R(T) n_e R(\Delta) (1+z)^3, \quad (35)$$

where $F_M(\Delta)$ is the mass fraction of the IGM occupied by regions with density less than Δ , \dot{n}_{ν} is the rate at which ionizing photons are introduced in the IGM by galaxies, n_e is the electron number density, $\alpha_R(T)$ is the temperature-dependent recombination rate and $R(\Delta)$ is the clumping factor of the IGM, which is related to the second moment of the IGM density distribution. The IGM mass fraction $F_M(\Delta)$ is given by

$$F_M(\Delta_{\text{crit}}) = \int_0^{\Delta_{\text{crit}}} d\Delta \Delta P(\Delta), \quad (36)$$

and the clumping factor is given by

$$R(\Delta_{\text{crit}}) = \int_0^{\Delta_{\text{crit}}} d\Delta \Delta^2 P(\Delta). \quad (37)$$

Reionization is said to be complete once all low-density regions (say, with overdensities $\Delta < \Delta_{\text{crit}} \sim 60$) are ionised. We refer to the redshift at which this happens as the redshift of reionization, z_{reion} . We follow the ionization and thermal histories of neutral and H II regions

simultaneously and self-consistently, treating the IGM as a multi-phase medium. We assume that helium is singly-ionized together with hydrogen and contributes to the photoionization heating. We do not consider the double ionization of helium, which is thought to have occurred at $z \sim 3$ (e.g., [Worseck et al. 2011](#)).

The rate of ionising photons injected by the galaxies into the IGM per unit time per unit volume at redshift z is denoted by $\dot{n}_{\text{ph}}(z)$, which is determined by the star formation rate. Using our star formation model described above, we can write the rate of emission of ionising photons per unit time per unit volume per unit frequency range, $\dot{n}_\nu(z)$, as

$$\dot{n}_\nu(z) = f_{\text{esc}} [N_\gamma^{\text{II}}(\nu)\Psi^{\text{II}}(z) + N_\gamma^{\text{III}}(\nu)\Psi^{\text{III}}(z)] \quad (38)$$

where f_{esc} is the escape fraction of UV photons, and $N_\gamma^{\text{II}}(\nu)$ and $N_\gamma^{\text{III}}(\nu)$ are the total number of ionising photons emitted per unit frequency range per unit stellar mass from Population I/II and Population III star forming halos respectively. These quantities are calculated by integrating the stellar spectra over an appropriate range. $\Psi^{\text{II}}(z)$ and $\Psi^{\text{III}}(z)$ are the cosmic Population I/II and Population III star formation rates. At any redshift,

$$\Psi(z) = \Psi^{\text{II}}(z) + \Psi^{\text{III}}(z). \quad (39)$$

The total rate of emission of ionising photons per unit time per unit volume, $\dot{n}_{\text{ph}}(z)$, is obtained by simply integrating Equation (38) over the correct frequency range. The hydrogen photoionization rate is then given by

$$\Gamma_{\text{HI}}(z) = (1+z)^3 \int_{\nu_0}^{\infty} d\nu \lambda(z, \nu) \dot{n}_\nu(z) \sigma(\nu), \quad (40)$$

where $\sigma(\nu)$ is the hydrogen photoionization cross-section, and $\lambda(z, \nu)$ is the redshift-dependent mean free path of UV photons. The mean free path is governed by the distribution of high density neutral clumps and reproduces the observed density of Lyman-limit systems at low redshift. The photoionization rate is used with the average radiative transfer equation to calculate the evolution of $Q_{\text{HII}}(z)$ in the pre-reionization universe, and that of $\Delta_{\text{crit}}(z)$ in the post-reionization universe. Note that this approach assumes ionization equilibrium and local absorption of UV photons.

The mean free path is defined as the average distance between high density regions of the inhomogeneous IGM. It can be written as ([Choudhury & Ferrara 2005](#))

$$\lambda(z) = \frac{\lambda_0}{[1 - F_V(\Delta_{\text{crit}})]^{2/3}}, \quad (41)$$

where $F_V(\Delta_{\text{crit}})$ is the volume fraction of the IGM occupied by regions with density less than Δ_{crit} , given by

$$F_V(\Delta_{\text{crit}}) = \int_0^{\Delta_{\text{crit}}} d\Delta P(\Delta), \quad (42)$$

where $P(\Delta)$ is the probability distribution function of IGM overdensities, taken to have a lognormal form ([Miralda-Escudé et al. 2000](#); [Choudhury & Ferrara 2005](#)). We take λ_0 to be proportional to the Jeans length (Equation 47),

$$\lambda_0 = \lambda_{\text{mfp},0} r_J, \quad (43)$$

and constrain the constant of proportionality, $\lambda_{\text{mfp},0}$, using the number of Lyman-limit systems at low redshift, which is related to the mean free path by

$$\frac{dN_{\text{LLS}}}{dz} = \frac{c}{\sqrt{(\pi)\lambda(z)H(z)(1+z)}}. \quad (44)$$

We assume that the mean free path is independent of the photon energy up to the ionization threshold of He II and is proportional to $(\nu/\nu_{\text{HeII}})^{1.5}$ at higher energies ([Choudhury & Ferrara 2005](#)).

The IGM temperature evolves as

$$\frac{dT}{dt} = -2H(z)T - \frac{T}{1+X_{\text{HI}}} \frac{dX_{\text{HI}}}{dt} + \frac{2}{3k_B n_b (1+z)^3} \frac{dE}{dt}, \quad (45)$$

where dE/dt is the total photoheating rate and X_{HI} is the H I fraction. The photoheating term accounts for heating by the UV background and cooling due to recombinations and Compton scattering of CMB photons. The IGM temperature governs the thermal feedback on galaxy formation by stopping gas inflow on halos with mass less than $M_{\text{min}}(z)$. We take this to be the Jeans mass, given by

$$M_{\text{min}} = \frac{4}{3} \pi r_J^3, \quad (46)$$

where r_J is the comoving Jeans length

$$r_J = \left[\frac{2k_B T \gamma}{8\pi G \rho_c m_p \Omega_m (1+z)} \right]^{1/2}, \quad (47)$$

where γ is the adiabatic index and m_p is the mass of the proton. Note that before reionization is complete, the H II regions are distinct. During this epoch, the temperature in H II regions is different from that in H I regions. The average temperature is then given by the mean of these two temperatures, weighted by $Q_{\text{HII}}(z)$. Similarly, both regions have different M_{min} . This is relevant in understanding the role that M_{min} plays in our star formation prescription above.

Note that in all of the above, we evolve two distinct sets of haloes corresponding to haloes forming in H I and H II regions respectively. Each set of haloes is affected by photoionization feedback differently as the temperatures of H I and H II regions are different. Any average property, such as the cosmic SFR, at a given redshift is an average of these two sets weighted by the volume filling fraction of H I and H II regions. This distinction is unimportant at redshift $z < z_{\text{reion}}$, when there are no H I regions anymore.

Given the above model, we obtain best-fit parameters by comparing with various observations such as the redshift evolution of photoionization rate obtained from the Ly α forest ([Bolton & Haehnelt 2007](#)), the electron scattering optical depth ([Hinshaw et al. 2012](#)), and the total baryon fraction in structures at $z = 0$ ([Fukugita & Peebles 2004](#)). These parameters are summarised in Table 2 along with their fiducial values and the constraints used to obtain them.

Before moving on to the results of our model, we compare our galaxy formation model with conventional semi-analytical models of galaxy formation used in the

Table 2
Free parameters in our model

Parameter	Fiducial value	Constraint
f_{esc}	0.04	τ_e and Γ_{HI}
f_* (Pop. II)	0.02	τ_e and Γ_{HI}
f_* (Pop. III)	0.04	τ_e and Γ_{HI}
$\lambda_{\text{mfp},0}$	1.7×10^{-3}	dN_{LLS}/dz
ϵ	1.0×10^{-6}	$f_{b,\text{struct}}(z=0)$
$f_{\text{gas,in}}$	0.7	Bouché et al. (2010)
ζ	Eq. (20)	Krumholz & Dekel (2012)
Z_{crit}	$10^{-4} Z_{\odot}$	–

literature (e.g., Kauffmann et al. 1999; Cole et al. 2000; De Lucia et al. 2004; Baugh 2006). The basic approach in these models is two-step: first, halo merger trees are constructed from N-body cosmological simulations; next, baryonic physics is calculated in each individual halo using prescriptions similar to those described above. When haloes merge, the stellar, gas, and metal masses are suitably combined, possibly with some extra prescriptions for events such as starbursts or active galactic nuclei (AGN). Our approach in modeling galaxy formation in this paper is also two-step. However, instead of drawing halo merger trees from N-body simulations, we only draw the average mass assembly histories of haloes. This is a significant reduction in information, as the average mass at redshift z of a halo with mass M at $z=0$ is the mean of the masses all progenitors at redshift z of all such haloes in the simulation box (see Fakhouri et al. 2010 for details of how this is done). In particular, by considering only the mean assembly histories, we lose any information regarding the intrinsic scatter in any property (such as halo mass, stellar mass, gas mass, or chemical abundance), even for fixed halo mass. Nonetheless, this simplification affords us the ability to calculate the IGM thermal and ionization histories and the evolution of H I and H II regions in the IGM by solving the average radiative transfer equation (Equation 35). It is not possible to do this in conventional merger-tree-based semi-analytic models.

Although our approach is different from conventional semi-analytic models, we expect our results to correspond to averaged results of those models. Thus, e.g., the stellar mass at a given redshift of a given halo of mass, say, M in our model, corresponds to the mean stellar mass of all haloes at that redshift in a merger-tree-based model. This can be seen from the agreement between our model predictions and observational data for average quantities such as cosmic star formation rate, gas phase metallicity, and mass-metallicity relation, as we discuss below.

3. RESULTS

3.1. Global properties of the chemical evolution models

Our model for galaxy and IGM evolution is constrained to produce the observed star formation rate (SFR) density evolution, the fraction of total baryon density in haloes at low redshift, and the reionization history of the IGM as measured by the Thomson scattering optical depth to the last scattering surface (τ_e) and the hydrogen photoionization rate (Γ_{HI}). Figure 1 shows the evolution of the cosmic SFR density. The solid curves show the prediction of our model and the red data points

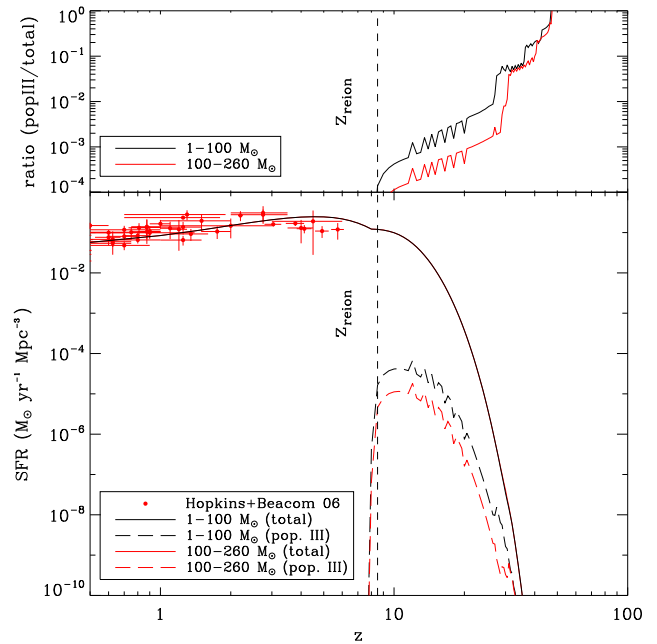


Figure 1. Evolution of the cosmic star formation rate (SFR) density in our models. In the bottom panel, solid and dashed curves show model prediction for the total and Population III SFR densities respectively. Black curves correspond to 1–100 M_{\odot} Population III IMF (model 1) and red curves to 100–260 M_{\odot} Population III IMF (model 3). Black and red solid curves are found to overlap at all redshifts. Data points are observational measurements from a compilation by Hopkins & Beacom (2006). In the top panel, we show the evolution of the ratio of Population III SFR to the total SFR. fractional contribution of Pop. III SFR to the total SFR. Dashed vertical line shows the redshift of reionization. The oscillatory features in the curves are numerical effects.

show observational measurements from a compilation by Hopkins & Beacom (2006). All three models reproduce the observed rise in the SFR between $z=0$ and $z \sim 3$. The total SFR prediction of the three models are virtually identical. As we discuss in detail below, this is because the contribution from Population III stars is very small. However, given the error bars on the measurements and the simplicity of our model, we consider the match to be adequate. Note that recent measurements of the SFR density at $z \sim 7-10$ by Bouwens et al. (2010) and Ellis et al. (2013) are smaller than our model prediction at these redshifts. These measurements report values of $\lesssim 10^{-2} M_{\odot} \text{ yr}^{-1} \text{ Mpc}^{-3}$ at $z \sim 8$ and $\lesssim 10^{-3} M_{\odot} \text{ yr}^{-1} \text{ Mpc}^{-3}$ at $z \sim 10$. Our values at both these redshifts $\gtrsim 10^{-2} M_{\odot} \text{ yr}^{-1} \text{ Mpc}^{-3}$. However, this discrepancy is because the SFR estimates of Bouwens et al. (2010) and Ellis et al. (2013) do not count the large contribution to the SFR by faint galaxies (which are more numerous). These estimates are obtained by integrating the UV luminosity functions down to $0.05L_{z=3}^*$. This limit corresponds to an AB magnitude of about -18 at 1500 \AA , while we find galaxies down to $\gtrsim -17$ in our model. In a forthcoming paper (Kulkarni et al., in prep.), we analyse this issue in detail and show that our model predictions are in good agreement with high-redshift SFR estimates when the faintness limit of Bouwens et al. (2010) and Ellis et al. (2013) is applied.

Figure 2 shows the thermal evolution of the IGM in our models in comparison with some observational measure-

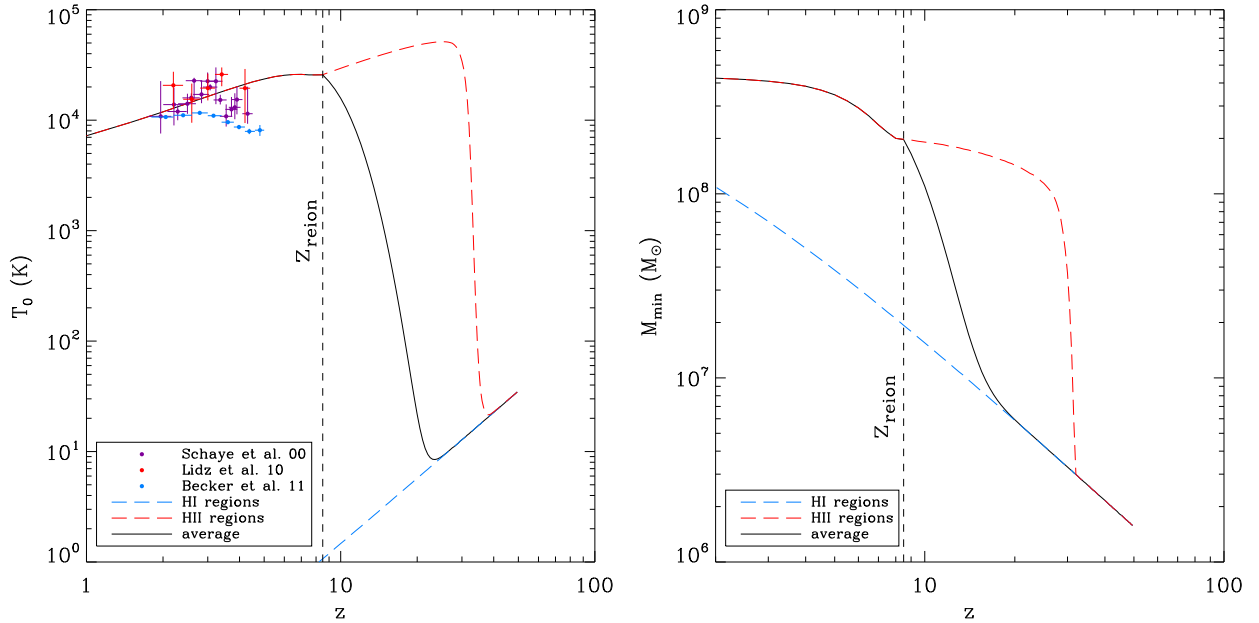


Figure 2. Evolution of IGM temperature (left panel) and the filtering mass (right panel) in our models, shown here for model 3. In both panels, the blue dashed curve shows the evolution in H I regions and the red dashed curve shows the evolution in H II regions. The average is shown by the solid black curve in both panels. Dashed vertical lines in both panels shows the redshift of reionization. Data points in the left panel are observational measurements of the IGM temperature from the Lyman- α forest (Schaye et al. 2000; Lidz et al. 2010; Becker et al. 2011).

ments (Schaye et al. 2000; Lidz et al. 2010; Becker et al. 2011). The solid curve in left panel shows the evolution of the temperature of the IGM at mean density (T_0), which is the temperature usually measured from absorption spectra of high redshift quasars. At redshift $z \gtrsim 20$, T_0 decreases adiabatically $\propto (1+z)^2$. However, as the H II regions around first galaxies form, this temperature gradually rises to about 2×10^4 K at $z = z_{\text{reion}} \sim 6$. Once reionization is complete, only the highest density regions in the IGM are left to be ionized. Thus the mean density regions evolve unaffected and T_0 then decreases to $\sim 10^4$ K. At redshift higher than z_{reion} , T_0 is the mean of temperatures in H I and H II regions, weighted by the volume filling factor. As a result, at these redshifts temperatures in these regions are more relevant. In Figure 2 (left panel), the red dashed curve shows the temperature evolution in H II regions, and the blue dashed curve shows the same in H I regions. The average H II region temperature climbs to a high value of a few times 10^4 K at $z \sim 20$ when the first sources turn on. However, this does not affect T_0 at these redshifts as the H II region volume filling factor is small. The average temperature in H I regions continues to decrease with time due to adiabatic cooling. Note that as we do not model He II reionization in this paper, our ability in matching the observational measurements is restricted. All observational measurements are made in the redshift range $z = 2-4$, which is believed to be the epoch of He II reionization. We also note in passing that, while the only source of heat in our model is photoionizations, the temperature measurements in the redshift range $z = 2-4$ are not precise enough to rule out other, exotic, sources (??????).

Recall that here the volume filling factor of H II regions is calculated according to Equation (35). Present observational constraints on this quantity are not very strong. However, several upper limits have been sug-

gested in the literature. These include: (1) a lower limit of $Q_{\text{HII}} \gtrsim 0.6$ derived by Ouchi et al. (2010) at $z = 6.6$ from the evolution of the number density of Lyman- α emitting galaxies, (2) an upper limit on Q_{HI} at $z = 5.5$ and 6 measured by Mesinger (2010) by counting dark pixels in quasar spectra, (3) a lower limit of $Q_{\text{HII}} \gtrsim 0.5$ inferred by McQuinn et al. (2007) at $z = 6.6$ from the lack of an increase in the clustering of Lyman- α emitting galaxies, (4) an upper limit of $Q_{\text{HII}} \lesssim 0.1$ inferred from the proximity zone of a $z = 7.1$ quasar by Bolton et al. (2011), and (5) an upper limit of $Q_{\text{HI}} \lesssim 0.5$ inferred by McQuinn et al. (2008) from the red damping wing of the Ly α absorption line in the spectrum of a $z = 6.3$ gamma-ray burst. Our model is consistent with all of these constraints as in our model reionization is complete by redshift $z = 8$.

The thermal evolution of the IGM dictates the evolution of M_{min} , the minimum mass of star-forming haloes, which is shown in the right panel in Figure 2. This quantity implements photoionization feedback in our model. As described in the previous section, we calculate M_{min} using a Jeans criterion. At a given redshift the minimum mass of star-forming haloes is either given by the atomic cooling threshold of 10^4 K, or by the local Jeans mass, whichever is higher. Other models of M_{min} are present in the literature, which take into account the full thermal history of the IGM instead of the instantaneous temperature (Gnedin 2000; Okamoto et al. 2008). We ignore these improvements and focus on the Jeans method for simplicity; this approximation does not affect our results strongly. The solid curve in Figure 2 (left panel) shows the average M_{min} evolution. It increases monotonically with decreasing redshift and is $\sim 2 \times 10^8 M_{\odot}$ at $z = z_{\text{reion}}$. It is $\sim 6 \times 10^8 M_{\odot}$ at redshift 1. It is important to note that this is only the average M_{min} ; the minimum mass is different in H I and H II regions. These are shown by the

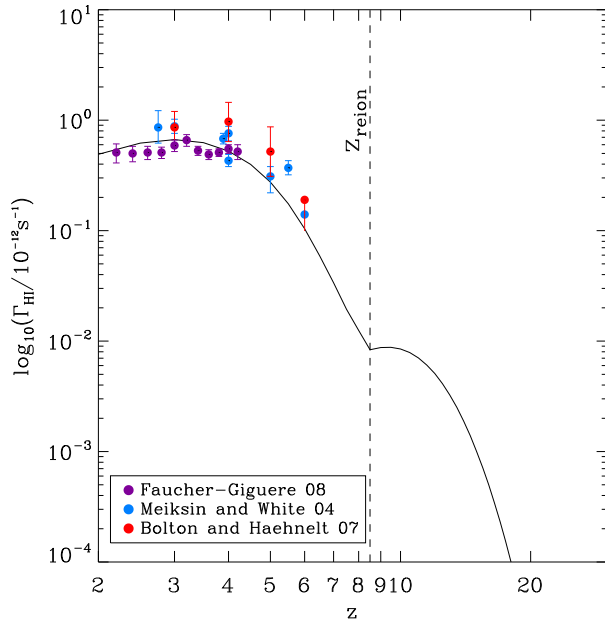


Figure 3. Hydrogen photoionization rate in our models (solid curve), compared with measurements from the Ly α forest. Blue data points show measurements by Meiksin & White (2004), red points are by Bolton & Haehnelt (2007), and magenta points are by Faucher-Giguère et al. (2008). Dashed vertical line shows the redshift of reionization.

blue and red curves in Figure 2. Thus, galaxies forming in these regions are affected differently. The minimum mass in H II region grows to about $10^8 M_{\odot}$ as soon as the first sources are turned on and the temperature of these regions is boosted to $\sim 10^4$ K. On the other hand, the minimum mass in H I regions increases much more slowly with decreasing redshift as it is always determined by the atomic cooling threshold alone. The relative contribution of the two regions to the solid black curve in Figure 2 is determined by the filling factor of H II regions. Of course, this distinction is not important in the post-reionization phase, where there are no H I regions.

As seen in the thermal evolution in Figure 2, IGM reionization in our model is gradual. This gradual change in the ionization state of the IGM helps us simultaneously reproduce the two most robust observational constraints on reionization: (1) the observed Thomson scattering optical depth to the last scattering surface $\tau_e = 0.089 \pm 0.014$ (Hinshaw et al. 2012), and (2) the measurements of the hydrogen photoionization rate, Γ_{HI} , from observations of the Ly α forest (Meiksin & White 2004; Bolton & Haehnelt 2007; Faucher-Giguère et al. 2008). The hydrogen photoionization rate in our model 3 is shown in Figure 3; our other models (1 and 2) give very similar results. The model prediction matches very well with the observational measurements. The photoionization rate increases rapidly as UV photon sources build up at $z > z_{\text{reion}}$. There is a sudden jump at $z = z_{\text{reion}}$ when different H II regions overlap. This is because at this redshift H II regions overlap and a given point in the IGM starts “seeing” multiple sources, which rapidly enhances the UV photon mean free path, thereby affecting the photoionization rate.

We now turn to the mass-metallicity relation prediction in our models, which is shown in Figure 4. The

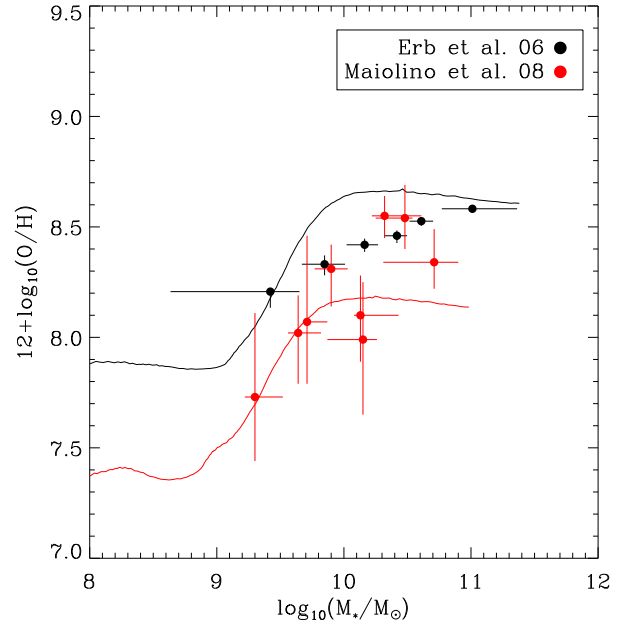


Figure 4. The mass-metallicity relation prediction from our models (solid curves) compared with observational measurements (data points). Measurements by Erb et al. (2006) at $z = 2.27$ are shown in black and those by Maiolino et al. (2008) at $z = 3.7$ are shown in red. Note that the amplitudes of mass-metallicity relations are uncertain and have been rescaled as described in the text.

mass-metallicity relation can be easily predicted in our model because for each halo mass, we calculate the stellar mass and gas-phase abundances of various metals at various redshifts, as explained above in section 2. In particular, in Figure 4, we compare the stellar mass with the oxygen abundance. We find that the model predictions match quite well with observations at $z = 2.27$ (Erb et al. 2006) and $z = 3.7$ (Maiolino et al. 2008). The oxygen abundance increases with stellar mass for galaxies in the intermediate mass range. At the high mass end ($M_* > 10^{11} M_{\odot}$) we find a slow decline in the oxygen abundance. This is because the gas accretion rate in these haloes is high, which results in dilution of their ISMs. Also, it is difficult for outflows to remove gas from the deeper potential wells of these halos. Note that the measurements of the mass-metallicity relationship are quite uncertain (Kewley & Ellison 2008; Krumholz & Dekel 2012). Therefore, to compare our estimate of metallicity to the observations we force the zero point of the predictions to match with that of the observations at $z = 2.27$. The model mass-metallicity relationship has a slightly different slope than the observational points at $z = 2.27$. However, given the simplicity of our model, and our focus on ratios of abundances in this work, we take the level of agreement to be sufficient. We will also see below that when the average ISM metallicity of galaxies is averaged agrees perfectly with the mean ISM metallicity inferred from observations of damped Ly α absorbers (DLAs).

In summary, our average galaxy formation and chemical evolution model is consistent with several observations, including the observed Thomson scattering optical depth to the last scattering surface, the observed hydrogen photoionization rate inferred from the Ly α forest, the slope of the mass-metallicity relation of galaxies at

Table 3
Logarithmic yields of different species in our three models, obtained by using Equation (48). Note that some yields, e.g., Fe and Si, do not have a monotonic dependence on stellar mass.

Species	Model 1	Model 2	Model 3
C	-2.34	-1.72	-1.51
N	-5.42	-6.12	-6.49
O	-1.59	-0.94	-0.58
Si	-3.04	-3.17	-1.29
Fe	-2.71	-4.31	-1.87
Zn	-5.95	-7.16	-6.98

various redshifts, and the evolution of cosmic star formation rate density. It also agrees well with the low-mass slope, characteristic mass, and normalization of the stellar-to-halo-mass relation, and, as we will show below, the evolution of the mean ISM metallicity inferred from observations of DLAs.

3.2. Effect of the Population III stellar IMF

To study how the Population III stellar IMF affects above results, we now consider three different Population III stellar IMFs shown in Table 1. Several early studies predicted that Population III stars have a characteristic mass of a few hundred M_{\odot} (e.g., Abel et al. 2002). In recent years, this prediction has come down in the range of 20–100 M_{\odot} (e.g., Turk et al. 2009). Recently, Dopcke et al. (2012) argued that in the absence of metal-line cooling, dynamical effects can still lead to fragmentation in proto-stellar gas clouds. In their simulations, this resulted in Population III stars with masses as low as 0.1 M_{\odot} . (This picture predicts the existence of many Population III stars surviving in the Galaxy till the present day.) Enrichment beyond Z_{crit} merely results in a change in the slope of the IMF, not in its mass values. Given this lack of certainty in our knowledge of the Population III IMF, in this work we choose to work with three different IMFs: 1–100 M_{\odot} Salpeter, 35–100 M_{\odot} Salpeter, and 100–260 M_{\odot} Salpeter. In each case, our Population II IMF is fixed to 0.1–100 M_{\odot} Salpeter. Each of these three models is calibrated independently, as described above. Our goal is to understand how the difference in these Population III scenarios is reflected in chemical evolution of galaxies. The 1–100 M_{\odot} and 100–260 M_{\odot} IMFs are selected to represent two extreme possibilities: if metal-free gas can fragment due to dynamical effects the IMF will favour small stellar masses, but in the absence of fragmentation Population III stars could have masses of the order of $\sim 100 M_{\odot}$. The intermediate (35–100 M_{\odot}) IMF is chosen to consider the effect of core collapse supernovae. If the distinct chemical signatures of these three IMFs turn out to be observable in high redshift galaxies, then such observations could act as a probe of the Population III IMF.

The contribution of Population III stars to the total cosmic SFR density is shown in Figure 1, in which the bottom panel shows the evolution of the Population III SFR ($\Psi^{\text{III}}(z)$) and the top panel shows the fractional contribution to the total SFR ($\Psi^{\text{III}}(z)/\Psi(z)$). Evidently, Population III stars contribute very little in terms of SFR. Furthermore, any Population III contribution is

essentially zero by redshift $z \sim 7$. The initial burst of Population III stars is sufficient to enhance the ISM metallicity beyond Z_{crit} in any halo mass bin. When this happens, the corresponding galaxy stops forming Population III stars. Since most of the mass in the universe is contained in M_* haloes, the globally averaged Population III SFR starts declining as soon as these haloes cross the Z_{crit} threshold. Since the IMF in model 1 has a lower metal yield than that in model 3, haloes take longer to cross the Z_{crit} threshold. Therefore, the Population III SFR contribution is larger in model 1. These results are in good agreement with the hydrodynamic simulations of Wise et al. (2012), who use only very massive Population III stars. We find that while the amplitude of the Population III SFR is sensitive to this effect, the lowest redshift with nonzero cosmic Population III SFR density is more dependent on the evolution of the minimum mass of star-forming haloes, M_{min} . Further, the small contribution of Population III stars to the global SFR is reflected in the fact that the effect of changing the Population III stellar IMF on the reionization and thermal history of the IGM is negligible in our model. As a result, the temperature evolution, as well as the photoionization rate evolution is practically independent of the Population III IMF.

However, we find that although the effect of Population III on the SFR and the IGM reionization and thermal history is small, it has a significant effect on the chemical properties of low mass galaxies. This is seen in Figure 5 (left column), which shows abundance ratios of various metal species as a function of halo mass at $z = 6$ for our three models. We focus on $[C/Fe]$, $[O/Si]$, $[Zn/Fe]$, and $[N/O]$. It is seen that in haloes with mass greater than a few times $10^9 M_{\odot}$, all four abundance ratios are constant, and equal to the Population II values. Changing the Population III IMF has no effect on the abundance ratios in these haloes. This is because in these haloes, Population III star formation has ceased at a much earlier time and the subsequent Population II star formation has wiped out any chemical signature of Population III star formation. The constancy of the abundance ratios is due to the fact that for a time-independent IMF, abundance ratios are equal to the ratio of corresponding chemical yields (Tinsley 1980; Pagel 2009). In low mass haloes, on the other hand, chemical signatures of Population III star formation have not yet been wiped out. As a result, abundance ratios in these haloes depend on the Population III IMF and are different in each of our Population III models. Thus, the chemical signature of Population III stars slowly emerges as we move towards low halo masses. Our model suggests that this is probably the best hope of constraining the Population III SFR density on cosmic time scale and the Population III IMF.

When we change the Population III model, the abundance ratios in low mass haloes change significantly. For example, the $[O/Si]$ ratio shows a change of more than 1 dex when we change from model 2 to model 3. This can be seen in Table 3, which shows the Population III yields of O and Si in all three models. Here, the yield of species i is defined as

$$y_i = \frac{\int dm \cdot \phi(m) \cdot m \cdot p_i(m)}{\int dm \cdot m \cdot \phi(m)}, \quad (48)$$

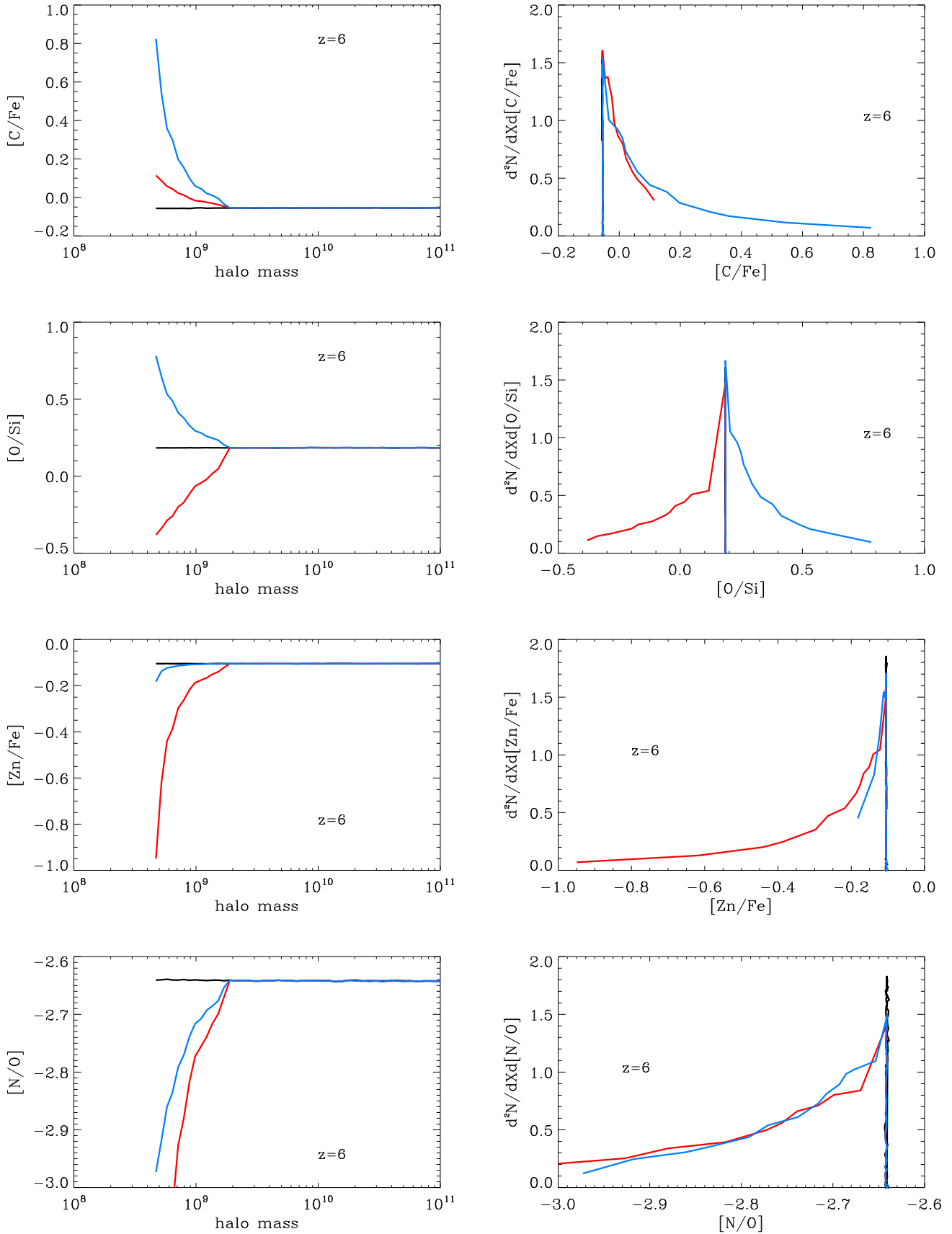


Figure 5. Abundance ratios and DLA distribution functions predicted by our model at $z = 6$. Panels in the left column shows the dependence of abundance ratios of halo mass in our model, while those in the right column show the predicted distribution of DLA abundance ratios. Black, blue and red curves correspond to models 1, 2, and 3 respectively.

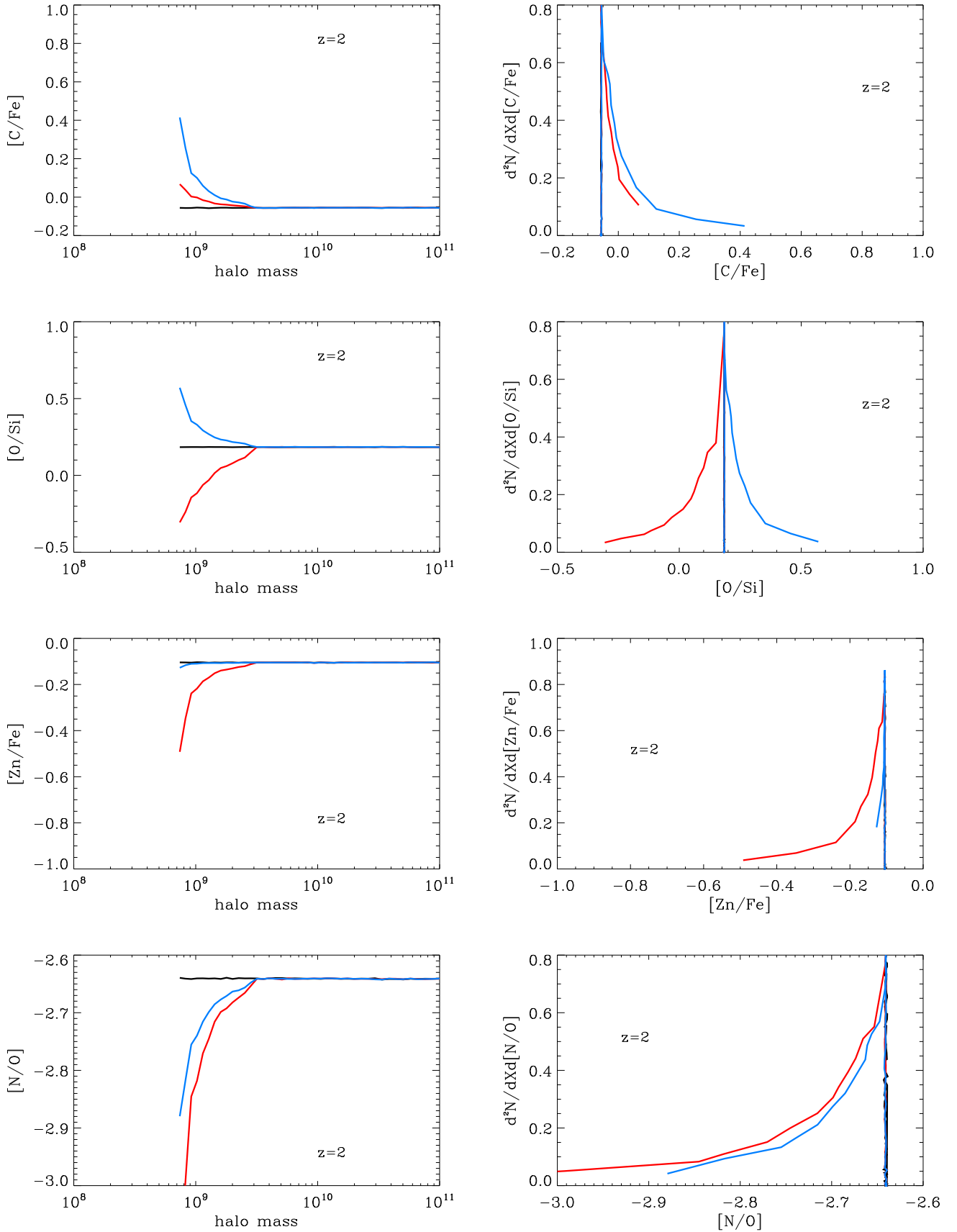


Figure 6. Abundance ratios and DLA distribution functions predicted by our model at $z = 2$, shown on the same scale as Figure 5. Columns are same as Figure 5. Black, blue and red curves correspond to models 1, 2, and 3 respectively. We see that the spread in the values of abundance ratios is reduced considerably at $z = 2$ as compared to $z = 6$.

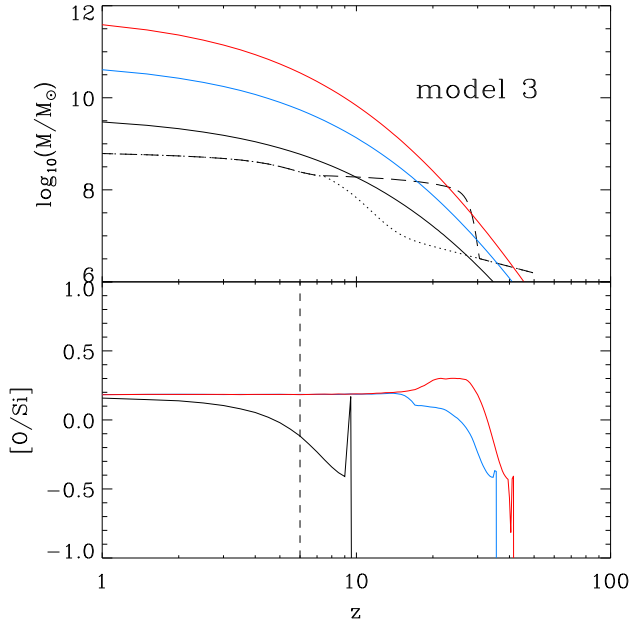


Figure 7. Comparison of chemical evolution in haloes with three different masses, shown here for model 3. The dashed line in the top panel shows the H II region filtering mass from Figure 2, whereas the dotted line shows the evolution of the average filtering mass scale. The black, red, and blue curves denote three different haloes. The dashed vertical line marks $z = 6$, which corresponds to the redshift in Figure 5. The spike in the plot is a result of the most massive stars in the model.

where $p_i(m)$ is the fraction of initial stellar mass m that is converted to species i . (Table 3 shows $\log(y_i)$.) The ratio of oxygen yield to silicon yield is comparable to solar in model 1.³ However, it is much lower than solar in model 3, and much higher than solar in model 2. This is because in model 3 high mass Population III stars produce large amounts of silicon during the O-burning process. This is reflected in the $[O/Si]$ ratio shown in Figure 5. Similar considerations explain the differences seen in other abundance ratios in low mass haloes in the three models. As we move towards lower redshift, we would expect to see the abundance ratio values to move away from their Population III values towards the Population II values even in small mass haloes. This is seen in Figure 6 (left column) which shows the same abundance ratios as Figure 5 at $z = 2$. The abundance ratio values in low mass haloes are much closer to the Population II values.

3.3. Why do low mass galaxies retain an imprint of Population III stars?

As described above, our model predicts that Population III stars will leave an imprint on the ratio of abundances of metals in low mass haloes, while any such imprint is wiped out in high mass haloes by subsequent Population II star formation. In this section, we discuss the reason behind this contrast between low mass and high mass haloes. In a nutshell, it is caused by a difference in Population III-to-II transition redshifts of

³ For a given element X, we define the abundance relative to the solar value in the usual way, i.e., $[X/Y] = \log_{10}(n_X/n_Y) - \log_{10}(n_X/n_Y)_\odot$, where n_i is the number density of element i . Solar photospheric abundance values are taken from Anders & Grevesse (1989).

these haloes, which in turn is a result of photoionization feedback.

The solid curves in Figure 7 (top panel) show the average growth of three different haloes from H II regions in one of our models (model 3). These haloes have masses of $10^{9.5} M_\odot$, $10^{10.5} M_\odot$, and $10^{11.5} M_\odot$ respectively at $z = 1$. Their growth is described by Equation 1. The dashed line in this panel shows the evolution of the filtering mass M_{\min} in H II regions in this model. It can be seen that the three haloes satisfy the star formation criterion, $M > M_{\min}$ at three different redshifts, approximately $z = 10$, 20 , and 25 respectively. Thus each halo forms its first stars, which are Population III, at very different times. This has an effect on the chemical evolution of these three mass bins, which is shown in the bottom panel of Figure 7. In this panel, the three solid curves show the evolution of $[O/Si]$ in the same halo mass bins as the top panel. (We still focus on model 3.) Since the Population III IMF in model 3 ($100\text{--}260 M_\odot$) produces negative values of $[O/Si]$, we expect a negative value of $[O/Si]$ in each halo mass bin when Population III stars form. However, as time progresses, Population II star formation takes over in each mass bin, because of which the value of $[O/Si]$ approaches $+0.2$. This is seen to happen in all three halo mass bins. However, this happens at *different redshifts* for different halo masses because they have different redshifts of Population III star formation (and therefore also the redshifts of Population III-to-II transition). The redshift at which Population III star formation first occurs is the redshift at which the condition $M > M_{\min}$ is first met, and is thus governed by the thermal feedback. As a result, at a given redshift, low mass haloes retain memory of their Population III enrichment history. This is highlighted by the vertical line marking $z = 6$ on the bottom panel of Figure 7. It can be seen that at this redshift, the two higher halo mass bins have already converged to $[O/Si] = 0.2$, but the lower mass bin still has $[O/Si] = -0.3$. It is this effect that causes the trends seen in Figure 6.

We now see why changing the Population III stellar IMF will selectively affect low mass haloes. Figure 8 shows the evolution of $[O/Si]$ for the same three haloes as Figure 7 in each of our three Population III models. As expected from the yields in Table 3, $[O/Si]$ for Population III stars in models 1 and 2 is greater than 0.2, but is less than 0.0 for model 3. The curves for models 1 and 2 show an enhancement in $[O/Si]$ during the first star formation episode in each halo mass bin. But this occurs at different redshifts for different halo masses, and explains the variation in the trends seen in Figure 6. An alternate way of understanding this is that in a closed system with a non-evolving IMF, all abundance ratios get locked at the value given by the ratio of their respective yields (Tinsley 1980; Pagel 2009)

$$\frac{Z_O}{Z_{Si}} = \frac{y_O}{y_{Si}}, \quad (49)$$

where the yields are defined in Equation (48). While this is strictly valid only under the instantaneous recycling approximation, it holds for real galaxies to a very good approximation (Tinsley 1980). As a result, abundance ratios will change only when there is a change in the IMF. This is exactly what happens when the stellar

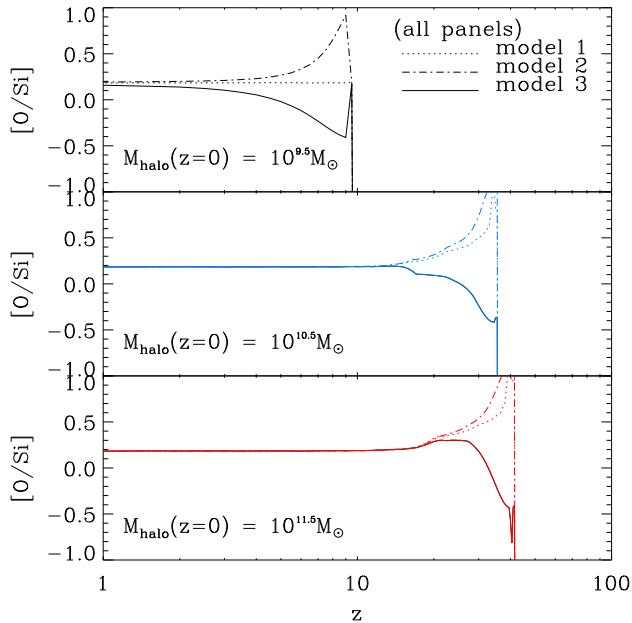


Figure 8. Evolution of $[O/Si]$ in our three models in the same three mass bins as in Figure 7, shown here in the same colours. The dotted, dot-dashed, and solid curves show evolution in models 1, 2, and 3 respectively.

IMF in a galaxy changes from Population III to Population II. For low-mass galaxies, this happens at a lower redshift. Therefore, they retain the Population III signatures at these redshifts. Note that the gas phase metallicity in these galaxies is greater than Z_{crit} , so they have already stopped forming Population III stars. Still, their relative abundances have not yet settled on the Population II values, and therefore carry a dependence on the Population III IMF.

It is often mentioned in the literature that an “odd-even” pattern in the abundances is a signature of Population III stars. This refers to the fact that in metal-free stars the production of species with odd nuclear charge is preferentially suppressed relative to their solar values. As we have seen above, the low mass haloes in our models retain memory of Population III star formation and therefore also show the odd-even pattern in elemental abundances. However, it is important to understand that odd-even pattern is not unique to Population III and also occurs in metal-poor Population II stars (Cooke et al. 2011). Hence the crucial point here is that one really wants to search for relative abundance trends which differ from the Population II predictions, and this information is encoded in low-mass halos.

3.4. Role of critical metallicity

In all of above, the critical metallicity Z_{crit} , at which a Population III IMF changes over to a Population II IMF, plays a crucial role. However, the value of Z_{crit} is currently a topic of debate (Klessen et al. 2012; Dopcke et al. 2012). When metallicity Z is greater than Z_{crit} , the availability of metal-line cooling and/or dust cooling is expected to lead to fragmentation in the ISM that could help form small mass stars with a Population II type IMF. In this paper, we have assumed $Z_{\text{crit}} = 10^{-4} Z_{\odot}$, a value motivated by most studies of fragmentation in metal-poor gas (Bromm et al.

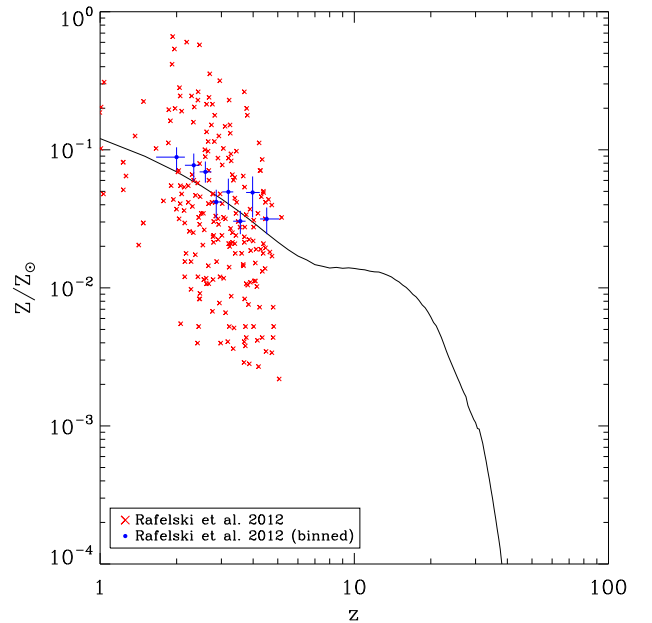


Figure 9. The “age-metallicity” relation in our model, which is given by an absorption cross section weighted average of gas phase metallicity of all mass bins. Red crosses are measurements of a sample of 241 DLAs by Rafelski et al. (2012). The blue points are mean values in different redshift bins, as presented by Rafelski et al. (2012). Vertical error bars on the blue points represent 1σ error bars.

2001; Bromm & Loeb 2003; Frebel et al. 2007). However, some studies have argued for a much smaller value of $Z_{\text{crit}} = 10^{-6} Z_{\odot}$ (Klessen et al. 2012). Since this number is not very well constrained, we comment on the effect on our results of variation in its value.

We find that values of Z_{crit} smaller than $10^{-4} Z_{\odot}$ have a very minor influence on our results. This is because in all three of our models, the metallicity of ISM in all haloes crosses Z_{crit} in a very short time after the first burst of Population III star formation. We explicitly checked this in our calculation by changing Z_{crit} to $10^{-5} Z_{\odot}$ and $10^{-6} Z_{\odot}$. In our models 2 and 3, in which the Population III metal yield is higher, there is no effect of a change in the critical metallicity. In model 1, lowering the critical metallicity to $10^{-6} Z_{\odot}$ has an effect of decreasing the average Population III SFR density, but only for $z > 20$. When Z_{crit} is lowered, haloes in this model take shorter time to stop forming Population III stars. These results are in qualitative agreement with those of Salvadori et al. (2007), who also found that the influence of Z_{crit} depends on the Population III stellar IMF. Given the negligible effect of changing Z_{crit} , we keep $Z_{\text{crit}} = 10^{-4} Z_{\odot}$ in this paper.

3.5. Observability as DLAs

As we saw above, low mass galaxies (halo masses $\sim 10^9 M_{\odot}$) at high redshift ($z \sim 6$) are likely to be useful in constraining Population III IMF and SFR. However, these galaxies are difficult to observe. Even otherwise, measurements of their relative abundances are unlikely to be accurate, as measurements from line emissions involve highly uncertain modeling of the observed H II regions. As a result, we need to look for an alternative method of observing these galaxies and measuring their metal

abundances. We now argue that damped Ly α systems (DLAs) in high-redshift quasar spectra provide just such an alternative.

DLAs represent H I reservoirs at high redshift. Metal abundances of DLAs have been measured up to $z = 6$. Using this data, an “age-metallicity relation” can be constructed for DLAs. Moreover, chemical abundance measurements in DLAs are very accurate. This is because in the cold H I reservoirs of DLAs, most metal species are in their singly ionised state, which can be probed in the optical from ground-based telescopes. Errors in DLA H I column density measurements are typically quite low, around 0.05 dex. Therefore errors in the corresponding metal abundance measurements ($[M/H]$) is also low, around 0.1 dex. Thus, observations of DLAs can be used to measure gas-phase metallicities at large cosmological lookback times with high precision (Wolfe et al. 2005). Furthermore, in DLAs, *relative abundances* can still be measured accurately deep into the reionization epoch ($z > 6$) using metal-line transitions redward of Ly α , even though Gunn-Peterson absorption precludes measurement of neutral hydrogen (cf. Becker et al. 2012).

In order to predict the properties of DLAs in our model, we assign a mass-dependent, physical, neutral hydrogen cross-section (“size”) to each halo, at every redshift. This assignment is performed using the fitting function

$$\Sigma(M) = \Sigma_0 \left(\frac{M}{M_0}\right)^2 \left(1 + \frac{M}{M_0}\right)^{\alpha-2}, \quad (50)$$

where the constants take the values of $\alpha = 0.2$, $M_0 = 10^{9.5} M_\odot$, and $\Sigma_0 = 40 \text{ kpc}^2$ at $z = 3$ (Pontzen et al. 2008; Font-Ribera et al. 2012). Values at other redshifts are calculated by mapping haloes at these redshifts to haloes $z = 3$ according to circular velocity (Font-Ribera et al. 2012). Our choice of the fitting function in Equation (50) is inspired by Pontzen et al. (2008), who find that it provides a good fit to absorption systems in their hydrodynamical simulation at $z = 3$. As another check on Equation (50), we look at the average evolution of ISM metallicities. The average gas-phase metallicity at a given redshift is

$$Z(z) = \frac{\int dm \cdot N(m, z) \cdot Z_{\text{ISM}}(m, z) \cdot \Sigma(m, z)}{\int dm \cdot N(m, z) \cdot \Sigma(m, z)}. \quad (51)$$

Figure 9 shows this quantity in comparison with metallicity estimates for 100 damped Ly α systems (DLAs) with $z \lesssim 4$ by Prochaska et al. (2003). Our models are in good agreement with the mean metallicities of the observed DLAs. It is encouraging that our results are also comparable to those of the recent hydrodynamical simulations (Cen 2012; Fumagalli et al. 2011; Davé et al. 2011).

For any measurable property p (such as metallicity, or abundance ratio) of DLAs, we can calculate the number of systems with different values of p in a sample of DLAs. This is called the line density distribution, and with Equation (50) in hand, it can be written as (e.g., Wolfe et al. 2005)

$$\frac{d^2 N}{dX dp} = N(M) \cdot \Sigma(M) \cdot \frac{dl}{dX} \frac{dM}{dp} \cdot (1+z)^3. \quad (52)$$

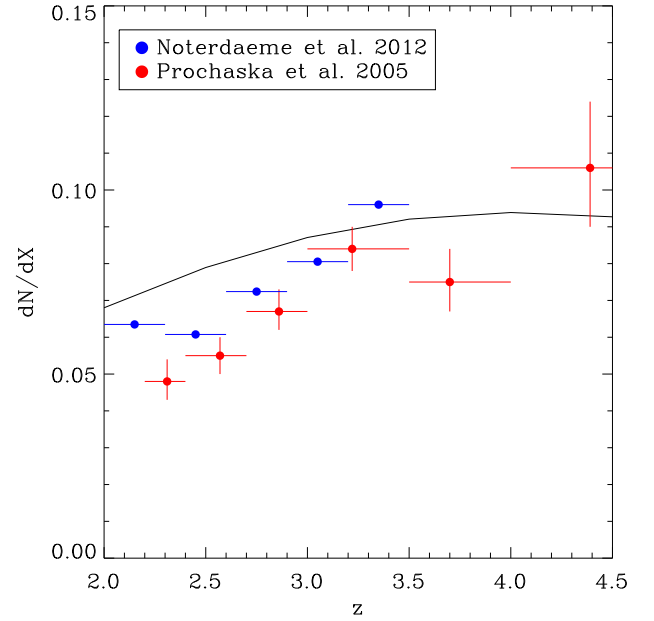


Figure 10. Evolution of dN/dX in our model. The blue and red data points are from measurements by Noterdaeme et al. (2012) and Prochaska et al. (2005) respectively.

Here, X is an absorption length element given by

$$\frac{dl}{dX} = \frac{c}{H_0(1+z)^3}, \quad (53)$$

$dl = c dt$ is a length element, and p is the property in consideration. The halo mass is denoted by M , $N(M)$ is the comoving number density of halos (i.e., the halo mass function), and $\Sigma(M)$ is the halo cross section given by Equation (50). The quantity dM/dp in Equation (52) can be easily calculated in our model, as properties like metallicity and relative abundances are known for all halo masses. The integral of Equation (52) over all values of p is just the total line density of DLAs, dN/dX . The evolution of dN/dX in our model is shown in Figure 10. Our results are in reasonable agreement with the values obtained from the Sloan Digital Sky Survey (SDSS) DR5 by Prochaska et al. (2005) and from SDSS DR9 by Noterdaeme et al. (2012). (Note that we have assumed a slightly smaller value of α compared to Pontzen et al. (2008) to get a good match to observed dN/dX .)

Using Equation (52), we plot the line density distribution of DLAs at $z = 6$ as a function of various metal abundance ratios in Figure 5 (right column). We focus on $[O/Si]$ for this discussion, which can be easily generalized for other ratios in Figure 5. The panel corresponding to $[O/Si]$ shows the DLA line density distribution for the three Population III IMFs considered in this paper (Table 1). The distribution corresponding to model 2 (35–100 M_\odot ; blue curve) is peaked at $[O/Si] = 0.2$ and has a tail spreading out to higher values up to $[O/Si] = 0.8$. The distribution corresponding to model 3 (100–260 M_\odot ; red curve) is also peaked at $[O/Si] = 0.2$, but has a tail spreading out to *lower* values down to $[O/Si] = -0.4$. Finally, model 1 (1–100 M_\odot) is simply a delta function at $[O/Si] = 0.2$. The line density distribution in this model has no tail; all DLAs have the same abundance ratio of $[O/Si] = 0.2$. This suggests that the distribution of rela-

tive abundance values in a sample of DLAs depends on the Population III IMF, at least at sufficiently high redshifts.

This dependence of the line density distribution on Population III IMF can be understood in terms of the dependence of halo relative abundances on the Population III IMF. We discussed the latter in sections 3.2 and 3.3 above, and in the left-hand column of Figure 5. Focusing again on $[\text{O}/\text{Si}]$, recall that most high-mass haloes had $[\text{O}/\text{Si}] = 0.2$, while low-mass haloes had different values of $[\text{O}/\text{Si}]$, depending on the Population III IMF. This same effect is reflected in the line density distribution in the right-hand column of Figure 5, since all of these haloes contribute to the line density distribution via Equation (52). Thus, e.g., as low-mass haloes in model 2 (35–100 M_{\odot} ; blue curve) have $[\text{O}/\text{Si}] > 0.2$, DLAs corresponding to these haloes form the tail that spreads towards these values. Similarly, in model 3 (100–260 M_{\odot} ; red curve), low-mass haloes have negative $[\text{O}/\text{Si}]$, which results in a tail in the DLA line density distribution that extends towards these values. Finally, in model 1 (1–100 M_{\odot}), all haloes have the same value of $[\text{O}/\text{Si}]$. As a result, the DLA line density is a delta function centered on this value (0.2) and has no tail. This also suggests that with decreasing redshift, as more and more haloes move to their Population II-producing phase, the DLA line density distribution will reduce its spread and move towards the Population II value. This is exactly what is seen as we move from $z = 6$ to $z = 2$, as shown in Figure 6 (right column).

In sum, Figure 5 displays the general result that *the distribution of DLAs in the abundance-ratio space at sufficiently high redshift is sensitive to the Population III IMF*. In the absence of Population III stars causing any change in stellar yields over time, this distribution will be a delta function in the abundance-ratio space (neglecting corrections for the impact of dust on relative abundances, which we discuss below). However, the addition of a new Population III stellar population with different chemical yields, spreads DLAs out in the abundance-ratio space. The shape of this spread can constrain the IMF of Population III stars, while its evolution can constrain the Population III SFR history. (Note that as discussed before in section 3.3 above, the gas phase metallicity of these DLAs is higher than Z_{crit} , similar to a vast majority of observed DLAs. Still their relative abundances have not yet settled on the Population II values. This results in a dependence on the Population III IMF.)

Further, to check whether this effect is detectable and to show that it can indeed be used to probe the Population III IMF, in Figure 11, we show a simulated data set of 10 $[\text{O}/\text{Si}]$ measurements at $z = 6$ taken from the DLA line density distribution corresponding to model 2 (35–100 M_{\odot} ; shown in the top panel of Figure 11 and also in Figure 5). This data set is produced by random sampling the predicted distribution of $[\text{O}/\text{Si}]$ values in the model, and adding a Gaussian error of 0.1 dex to each sample point. An error of 0.1 dex corresponds to the typical accuracy with which abundance ratios in DLAs are measured (e.g., Becker et al. 2012). Using a KS test, we find that this sample rejects the Population II distribution at 4σ ($D = 0.9$, $p = 0.00017$). A set of 100 samples (each of size 10 and a Gaussian error of 0.1 dex) preferred the Population III IMF at

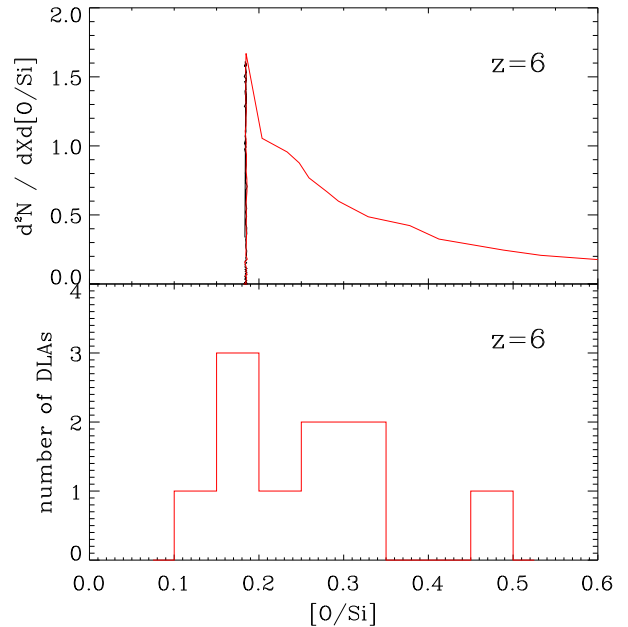


Figure 11. Top panel shows the predicted distribution of $[\text{O}/\text{Si}]$ values for Population II (black) and Population III (red; model 2) at $z = 6$. (This distribution is taken from Figure 5.) The bottom panel shows a histogram of a random sample of 10 $[\text{O}/\text{Si}]$ measurements taken from the Population III distribution in the top panel. An additional Gaussian error of 0.1 dex is added to each sampled point. A KS test shows that this sample rejects the Population II distribution at approximately 4σ ($D = 0.9$, $p = 0.00017$). This suggests that it is possible to detect the effect of Population III star formation even with a relatively small sample of DLA abundance ratio measurements with an accuracy of about 0.1 dex.

3.8σ on average ($\langle D \rangle = 0.8$, $\langle p \rangle = 0.007$). This suggests that the effects of Population III IMF on DLA abundance ratio are significant enough to be detectable with just 10 measurements accurate to about 0.1 dex⁴. A larger sample of 20 measurements rejects the Population II distribution at an even higher significance of about 5σ ($\langle D \rangle = 0.85$, $\langle p \rangle = 10^{-5}$; again assuming an accuracy of 0.1 dex). Note that this test used a single abundance ratio ($[\text{O}/\text{Si}]$). In practice, using multiple ratios as shown in Figure 5 can further improve the significance of the constraints. Also note that the metallicity of these low mass halos ($M \sim 10^9 M_{\odot}$) with Population III signatures is high enough to produce detectable lines at $z \sim 6$. For example, we can estimate the O I column density by (Salvadori & Ferrara 2012)

$$N_{\text{OI}} = \frac{3}{2\pi} \frac{M_{\text{O}}/\mu_{\text{O}}m_p}{\alpha^2 r_{\text{vir}}^2}, \quad (54)$$

where μ_{O} is the atomic weight of oxygen and $r = \alpha r_{\text{vir}}$ is the gas radius, where usually $\alpha \sim 0.8$ (Salvadori & Ferrara 2012). The oxygen mass M_{O} is calculated in each halo in our chemical evolution model. This gives $N_{\text{OI}} > 10^{15} \text{ cm}^{-2}$ for $\alpha = 0.8$. This value of the column density is already higher than that measured in several $z = 6$ DLAs by Becker et al. (2012), which span the range $N_{\text{OI}} = 10^{13.49} - 10^{14.47} \text{ cm}^{-2}$.

⁴ Any effects of dust depletion could in principle be higher than 0.1 dex. However, the scatter in observations at low redshift ($z \sim 2$) is less than 0.2 dex (Becker et al. 2012), which suggests that our results are valid even when effects of dust are included.

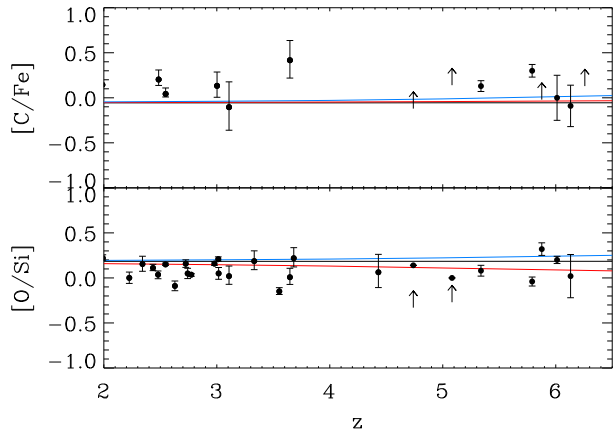


Figure 12. Evolution of the *average* values of $[C/Fe]$ and $[O/Si]$ in our models. The black, blue, and red curves correspond to models 1, 2, and 3 respectively. Data points show relative abundances in DLAs from a compilation by Becker et al. (2012). It is seen that changing the Population III IMF has little effect on the average values of relative abundances. However, the effect on the distribution of abundance ratio values is significant and detectable, as shown in Figure 11. This shows that it is the distribution of measurements that probes the stellar IMF and not the mean value of the measurements.

It is important to understand that the *distribution* of relative abundance values at high redshifts is used here, not the mean value at those redshifts. In fact, as we have seen, all line density distributions in Figure 5 are anchored on the Population II values of the respective abundance ratios. This is because even at high redshift, high mass haloes have already moved to their Population II star forming stage; only low mass haloes are expected to carry the memory of their Population III enrichment. Therefore, we expect the mean value of these any abundance ratio to be close to the Population II value. It will have very little dependence on the Population III IMF. This can be understood by explicitly calculating the mean value of different abundance ratios, given by

$$\langle p \rangle = \int \frac{d^2 N}{dX dp} \cdot p \cdot dp \cdot dX, \quad (55)$$

where $p = [M_1/M_2]$ is the abundance ratio of two species M_1 and M_2 , and dX is defined in Equation (53). Figure 12 shows the mean value of $[C/Fe]$ and $[O/Si]$ calculated in this fashion, corresponding to our three Population III models. Observational measurements of several DLAs from Becker et al. (2012) are also shown. It is seen that the average values predicted by our model are consistent with the observations, regardless of the Population III IMF used. (Note that the observational data shown here is uncorrected for effects of dust depletion.) The most striking feature in Figure 12 is the lack of evolution over the large redshift range from $z \gtrsim 6$ to $z \sim 2$. This is explained in our model by the fact that all large haloes show constant abundance ratios, corresponding to Population II. A second feature of Figure 12 is that varying the Population III IMF results in only a small change in the average value of the abundance ratio, as expected. It is only when we look at the spread of these values at different redshift that the effect of Population III IMF becomes visible.

4. DISCUSSION

We have shown that a chemical evolution model that also incorporates global effects like reionization and photoionization feedback is consistent with a wide range of possible Population III IMFs. However, this approach uncovers patterns in the metallicity distribution of high redshift galaxies which could potentially be useful in ruling out some Population III IMFs and SFRs.

It is therefore important to understand the domain of validity of our model. Matteucci & Calura (2004) and Calura et al. (2009) have studied the evolution of the mass-metallicity relation and the chemical properties of systems like dwarf galaxies using chemical evolution modelling of the kind that we have used here. They find that if the instantaneous recycling approximation is avoided, an approach that correctly incorporates effects of outflows and inflows successfully reproduces all observed chemical properties of galaxies. De Lucia et al. (2004) and De Lucia & Borgani (2012) have also used a similar chemical evolution model in their semi-analytic model of galaxy formation that fits several key observations very well. Furthermore, we focus on abundance ratios in this paper, which are more robustly predictable, given their simple dependence on the stellar IMF. Thus, given the uncertainties in high redshift observations and the simplicity of our model, the main conclusion of this paper regarding chemical signatures of Population III stars in high redshift galaxies is robust.

A second uncertainty in our calculation is the prescription used for photoionization feedback. Firstly, we have used a simple Jeans prescription whereas it has been argued that more detailed prescriptions give a better fit to hydrodynamical simulations (Gnedin 2000; Okamoto et al. 2008). However, the difference between these feedback prescriptions is small, especially at $z \gtrsim 5$ (Barkana & Loeb 2001). A detailed understanding of radiative feedback in galaxy formation is yet to emerge, primarily because of the large variety of approximations used in earlier work (Ciardi & Ferrara 2005). However the general consensus is that such a filtering scale increases from roughly $10^7 M_\odot$ at $z = 10$ to $10^9 M_\odot$ at redshift $z = 6$. This is in good agreement with the values we obtain in our study. A tentative observational evidence of such effect is seen in “dark” dwarf galaxies in the vicinity of high redshift AGN (Cantalupo et al. 2012) and in the difference between the evolution of star formation rate in low mass galaxies and that in high mass galaxies (Weinmann et al. 2012). Some authors have used simple fitting functions for M_{\min} that agree quite well with our evolution of M_{\min} (Salvadori & Ferrara 2012). A similar approach has also been used in semi-analytical models of galaxy formation (e.g., Baugh 2006). It should also be noted that the evolution of M_{\min} for $z \lesssim 5$ is not important for our present study as by such low redshift the contribution of Population III stars to chemical evolution is negligible.

Thirdly, our approach of evolving haloes and galaxies *in the mean* does not provide us with information regarding the scatter around the distributions shown here. However, we note that semi-analytic models based on halo merger trees find quite small scatter around the mean distributions of metallicities (around 1 dex at redshift 0; De Lucia et al. 2004). Further, scatter does not

affect abundance ratios; it can only affect the star formation histories of individual haloes. Therefore the effect of scatter on our central prediction, that distribution of DLA abundance ratios probe Population III IMFs, will be nearly zero. For example, positive values of [O/Si] at high redshift are inconsistent with Population III stars in the PISN range. Observations of these systems would be a strong argument against high mass Population III stars, regardless of the scatter in the observations, which will not affect the [O/Si] ratio. In fact, we want to highlight the fact that in this respect this approach of constraining Population III scenarios from observations of high redshift DLAs is possibly better than constraining them using observations of metal-poor stars in the Galactic halo. The metallicity distribution of metal-poor stars is highly dependent on the peculiar assembly history of the Milky Way, which is not guaranteed to follow the “average” assembly history that models require in order to constrain Population III SFR and IMF. As such, metal-poor stars are useful only if they unambiguously show the signature of a pair instability supernova. However, even in this case they will only provide indication of a single Population III star of a certain mass, not of the whole IMF or SFR.⁵ Similar arguments hold for observations of dwarf spheroidals and ultra-faint dwarfs.

We have assumed a constant UV photon escape fraction while calculating the IGM reionization history. This can potentially affect our conclusions if the escape fraction in Population III star forming haloes is so large that reionization constraints begin restricting Population III star formation parameter space. Indeed, it has been argued that the escape fraction will have a strong increasing evolution with redshift (Kuhlen & Faucher-Giguère 2012; Mitra et al. 2012). Also, the escape fraction could potentially have different values for galaxies with Population II and Population III star formation due to different spectral indices (Choudhury & Ferrara 2006). However, our assumption about the escape fraction is unlikely to affect our results significantly since we find that Population III stars do not contribute much to reionization due to their early termination. Thus, the reionization history affects our conclusions only moderately. Note that the value of escape fraction used in our model is comparable to that deduced from luminosity function measurements in recent studies (Mitra et al. 2012).

Finally, we comment about the role of dust. Dust affects the metal evolution of galaxies by preferentially depleting certain species like iron. We have not taken this effect into account. As such our results are only “production-side” estimates of the chemical abundance patterns. Dust obscuration is ignored in most DLA studies (Wolfe et al. 2005). This difficult problem can be alleviated by focusing on non-refractory species such as zinc and oxygen, which are not depleted on dust grains. We can also focus on “secondary elements” like nitrogen that depend on the square of the metallicity, which increases their sensitivity to underlying chemical enrichment patterns. We defer a detailed study of the effect of dust depletion to a future work. There is however, an empirical reason why dust depletion may have very little effect

on our main result. This is because it has been noted that dust depletion is strongly dependent on metallicity such that low metallicity systems have very little dust (Vladilo 2004; Becker et al. 2012; Rafelski et al. 2012). This combined with the observed metallicity evolution shown in Figure 9 suggests that there is very little dust in DLA at $z \sim 5$. Furthermore, Rafelski et al. (2012) report a sudden decrease in DLA metallicity at $z > 4.7$ (at low significance), which if real would further reduce the role of dust in these systems.

5. CONCLUSIONS

Our results are as follows:

- We have developed a chemical evolution model of galaxies that is consistent with a variety of global observational constraints on galaxy and IGM evolution, such as the cosmic SFR density evolution, IGM thermal evolution, and hydrogen photoionization rate evolution. We calculate the minimum mass of star forming galaxies self-consistently. This model produces galaxies that lie on observational curves such as the stellar-to-halo mass relation at low redshift and the mass-metallicity relation. We then explore influence of Population III stars on the predictions of this model, by varying the Population III stellar IMF.
- We find that different Population III stellar IMFs result in very different abundance ratio distributions in low mass galaxies (halo mass $\lesssim 10^9 M_\odot$) at high redshift. This is because photoionization feedback suppresses star formation in these galaxies till low enough redshift ($z \sim 10$), and memory of the initial generation of Population III stars is retained. For some ratios, e.g., [O/Si], the variation is as large as 1 dex. This variation is much greater than the uncertainty in metallicity measurements in DLAs. This effect is strong at redshift $z \gtrsim 5$ and grows weaker at lower redshift due to subsequent Population II star formation.
- The influence of Population III star formation is seen only in low-mass haloes. Changing the Population III IMF has no effect on the abundance ratio in high mass haloes. This is as expected since in these haloes abundance ratios are determined by Population II stars alone. It is only as we move downwards in halo mass that the Population III signature starts dominating.
- We modelled low-mass haloes as DLAs by assigning them a mass-dependent H I absorption cross-section. This model agrees with the observed metallicity-redshift relation for DLAs and the observed DLA line density evolution as a function of redshift. Using this model, we predict the line density distributions of DLAs as a function of different abundance ratios. We find that these distributions are anchored towards the Population II values of abundance ratios, but they show a significant dependence on the Population III IMF for $z \gtrsim 5$. This dependence is reduced at lower redshift due to subsequent Population II star formation.

⁵ Another way in which metal-poor stars can be of use is if we find a truly metal-free star. But this is difficult given the observational limitations (Frebel & Norris 2011).

- The dependence of the DLA line density distribution on Population III suggests that the distribution of DLAs in abundance-ratio space at sufficiently high redshift can provide very good constraints on Population III properties. The form of this distribution can constrain the IMF of Population III stars, while its evolution can constrain the global Population III SFR history. This constraint on Population III could possibly be stronger than constraints from other probes such as metal-poor stars and individual metal-poor DLAs. A simulated data set of just 10 DLAs at $z \sim 6$ measured with realistic accuracy is able to constrain specific Population III IMFs with high confidence. This method of probing Population III stars does not rely on the measurement of the H I column density. It is therefore useful at high redshift where Gunn-Peterson absorption precludes measurement of neutral hydrogen. Relative abundances can still be measured accurately in this epoch using transitions redward of Ly α , and self-shielded systems can be selected based on the presence of O I.
- Not only can the abundance ratio distributions distinguish between high-mass and low-mass Population III IMFs, they can also discriminate between different low mass Population III IMFs. For example, the two low mass Pop III IMFs that we consider in this paper are clearly distinguished by their oxygen abundance patterns.

ACKNOWLEDGEMENTS

We would like to acknowledge useful discussions with Carlton Baugh, T. Roy Choudhury, Gabriella De Lucia, Andrea Macciò, J. Xavier Prochaska, Marc Rafelski, Hans-Walter Rix, Stefania Salvadori, R. Srianand, and members of the ENIGMA group at MPIA, especially Gábor Worseck and Neil Crighton. We also thank the anonymous referee for several constructive comments that improved our presentation. GK would also like to thank Institut d'Astrophysique de Paris for hospitality. This work was partly supported by the French Agence Nationale pour la Recherche (ANR) within the Investissements d'Avenir programme under reference ANR-11-IDEX-0004-02 and via the grant VA-COUL (ANR-2010-BLAN-0510-01).

REFERENCES

- Abel, T., Bryan, G. L., & Norman, M. L. 2002, *Science*, 295, 93
- Anders, E., & Grevesse, N. 1989, *Geochim. Cosmochim. Acta*, 53, 197
- Barkana, R., & Loeb, A. 2001, *Phys. Rep.*, 349, 125
- Bauermeister, A., Blitz, L., & Ma, C.-P. 2010, *ApJ*, 717, 323
- Baugh, C. M. 2006, *Reports on Progress in Physics*, 69, 3101
- Becker, G. D., Bolton, J. S., Haehnelt, M. G., & Sargent, W. L. W. 2011, *MNRAS*, 410, 1096
- Becker, G. D., Sargent, W. L. W., Rauch, M., & Carswell, R. F. 2012, *ApJ*, 744, 91
- Bolton, J. S., & Haehnelt, M. G. 2007, *MNRAS*, 382, 325
- Bolton, J. S., Haehnelt, M. G., Warren, S. J., Hewett, P. C., Mortlock, D. J., Venemans, B. P., McMahon, R. G., & Simpson, C. 2011, *MNRAS*, 416, L70
- Bouché, N., et al. 2010, *ApJ*, 718, 1001
- Bouwens, R. J., et al. 2010, *ApJ*, 709, L133
- Bromm, V., Ferrara, A., Coppi, P. S., & Larson, R. B. 2001, *MNRAS*, 328, 969
- Bromm, V., & Larson, R. B. 2004, *ARA&A*, 42, 79
- Bromm, V., & Loeb, A. 2003, *Nature*, 425, 812
- . 2006, *ApJ*, 642, 382
- Bromm, V., & Yoshida, N. 2011, *ARA&A*, 49, 373
- Caffau, E., et al. 2011, *Nature*, 477, 67
- Calura, F., Pipino, A., Chiappini, C., Matteucci, F., & Maiolino, R. 2009, *A&A*, 504, 373
- Cantalupo, S., Lilly, S. J., & Haehnelt, M. G. 2012, *MNRAS*, 425, 1992
- Cen, R. 2012, *ApJ*, 748, 121
- Choudhury, T. R., & Ferrara, A. 2005, *MNRAS*, 361, 577
- . 2006, *MNRAS*, 371, L55
- Ciardi, B., & Ferrara, A. 2005, *Space Sci. Rev.*, 116, 625
- Cole, S., Lacey, C. G., Baugh, C. M., & Frenk, C. S. 2000, *MNRAS*, 319, 168
- Cooke, R., Pettini, M., Steidel, C. C., Rudie, G. C., & Nissen, P. E. 2011, *MNRAS*, 417, 1534
- Daddi, E., et al. 2010, *ApJ*, 714, L118
- Daigne, F., Olive, K. A., Silk, J., Stoehr, F., & Vangioni, E. 2006, *ApJ*, 647, 773
- Davé, R., Finlator, K., & Oppenheimer, B. D. 2012, *MNRAS*, 421, 98
- Davé, R., Oppenheimer, B. D., & Finlator, K. 2011, *MNRAS*, 415, 11
- De Lucia, G., & Borgani, S. 2012, *MNRAS*, 426, L61
- De Lucia, G., Kauffmann, G., & White, S. D. M. 2004, *MNRAS*, 349, 1101
- Dekel, A., et al. 2009, *Nature*, 457, 451
- Dopcke, G., Glover, S. C. O., Clark, P. C., & Klessen, R. S. 2012, *ArXiv e-prints*
- Ellis, R. S., et al. 2013, *ApJ*, 763, L7
- Erb, D. K. 2008, *ApJ*, 674, 151
- Erb, D. K., Shapley, A. E., Pettini, M., Steidel, C. C., Reddy, N. A., & Adelberger, K. L. 2006, *ApJ*, 644, 813
- Fakhouri, O., Ma, C.-P., & Boylan-Kolchin, M. 2010, *MNRAS*, 406, 2267
- Faucher-Giguère, C.-A., Lidz, A., Hernquist, L., & Zaldarriaga, M. 2008, *ApJ*, 688, 85
- Font-Ribera, A., et al. 2012, *ArXiv e-prints*
- Frebel, A. 2011, in *Bulletin of the American Astronomical Society*, Vol. 43, American Astronomical Society Meeting Abstracts 217, 329.01
- Frebel, A., Johnson, J. L., & Bromm, V. 2007, *MNRAS*, 380, L40
- Frebel, A., & Norris, J. E. 2011, *ArXiv e-prints*
- Fukugita, M., & Peebles, P. J. E. 2004, *ApJ*, 616, 643
- Fumagalli, M., Prochaska, J. X., Kasen, D., Dekel, A., Ceverino, D., & Primack, J. R. 2011, *MNRAS*, 418, 1796
- Fumagalli, M., et al. 2012, *ApJ*, 757, L22
- Genel, S., et al. 2008, *ApJ*, 688, 789
- Gnedin, N. Y. 2000, *ApJ*, 542, 535
- Heger, A., & Woosley, S. E. 2002, *ApJ*, 567, 532
- Hinshaw, G., et al. 2012, *ArXiv e-prints*
- Hopkins, A. M., & Beacom, J. F. 2006, *ApJ*, 651, 142
- Kauffmann, G., Colberg, J. M., Diaferio, A., & White, S. D. M. 1999, *MNRAS*, 303, 188
- Kewley, L. J., & Ellison, S. L. 2008, *ApJ*, 681, 1183
- Klessen, R. S., Glover, S. C. O., & Clark, P. C. 2012, *MNRAS*, 421, 3217
- Krumholz, M. R., & Dekel, A. 2012, *ApJ*, 753, 16
- Krumholz, M. R., & Thompson, T. A. 2007, *ApJ*, 669, 289
- Kuhlen, M., & Faucher-Giguère, C.-A. 2012, *MNRAS*, 423, 862
- Leitherer, C., et al. 1999, *ApJS*, 123, 3
- Levesque, E. 2012, in *-Ray Bursts 2012 Conference (GRB 2012)*
- Lidz, A., Faucher-Giguère, C.-A., Dall'Aglio, A., McQuinn, M., Fechner, C., Zaldarriaga, M., Hernquist, L., & Dutta, S. 2010, *ApJ*, 718, 199
- Loeb, A. 2010, *How Did the First Stars and Galaxies Form?*
- Mac Low, M.-M., & Ferrara, A. 1999, *ApJ*, 513, 142
- Maeder, A., & Meynet, G. 1989, *A&A*, 210, 155
- Maiolino, R., et al. 2008, *A&A*, 488, 463
- Matteucci, F., & Calura, F. 2004, *Ap&SS*, 294, 29
- . 2005, *MNRAS*, 360, 447
- McQuinn, M., Hernquist, L., Zaldarriaga, M., & Dutta, S. 2007, *MNRAS*, 381, 75
- McQuinn, M., Lidz, A., Zaldarriaga, M., Hernquist, L., & Dutta, S. 2008, *MNRAS*, 388, 1101
- Meiksin, A., & White, M. 2004, *MNRAS*, 350, 1107

- Mesinger, A. 2010, MNRAS, 407, 1328
- Miralda-Escudé, J., Haehnelt, M., & Rees, M. J. 2000, ApJ, 530, 1
- Mitra, S., Ferrara, A., & Choudhury, T. R. 2012, MNRAS, L1
- Neistein, E., & Dekel, A. 2008, MNRAS, 383, 615
- Noterdaeme, P., et al. 2012, A&A, 547, L1
- Okamoto, T., Gao, L., & Theuns, T. 2008, MNRAS, 390, 920
- Ouchi, M., et al. 2010, ApJ, 723, 869
- Pagel, B. E. J. 2009, Nucleosynthesis and Chemical Evolution of Galaxies
- Pan, T., Kasen, D., & Loeb, A. 2012a, MNRAS, 422, 2701
- Pan, T., Loeb, A., & Kasen, D. 2012b, MNRAS, 423, 2203
- Pontzen, A., et al. 2008, MNRAS, 390, 1349
- Prochaska, J. X., Gawiser, E., Wolfe, A. M., Castro, S., & Djorgovski, S. G. 2003, ApJ, 595, L9
- Prochaska, J. X., Herbert-Fort, S., & Wolfe, A. M. 2005, ApJ, 635, 123
- Rafelski, M., Wolfe, A. M., Prochaska, J. X., Neeleman, M., & Mendez, A. J. 2012, ApJ, 755, 89
- Rollinde, E., Vangioni, E., Maurin, D., Olive, K. A., Daigne, F., Silk, J., & Vincent, F. H. 2009, MNRAS, 398, 1782
- Salvadori, S., & Ferrara, A. 2009, MNRAS, 395, L6
- , 2012, MNRAS, 421, L29
- Salvadori, S., Schneider, R., & Ferrara, A. 2007, MNRAS, 381, 647
- Schaerer, D. 2002, A&A, 382, 28
- Schaye, J., Theuns, T., Rauch, M., Efstathiou, G., & Sargent, W. L. W. 2000, MNRAS, 318, 817
- Spite, M., Caffau, E., Bonifacio, P., Spite, F., Ludwig, H.-G., PLEZ, B., & Christlieb, N. 2013, ArXiv e-prints
- Springel, V., & Hernquist, L. 2003, MNRAS, 339, 312
- Tinsley, B. M. 1980, Fund. Cosmic Phys., 5, 287
- Turk, M. J., Abel, T., & O’Shea, B. 2009, Science, 325, 601
- Turk, M. J., Oishi, J. S., Abel, T., & Bryan, G. L. 2012, ApJ, 745, 154
- Vázquez, G. A., & Leitherer, C. 2005, ApJ, 621, 695
- Vladilo, G. 2004, A&A, 421, 479
- Weinmann, S. M., Pasquali, A., Oppenheimer, B. D., Finlator, K., Mendel, J. T., Crain, R. A., & Macciò, A. V. 2012, MNRAS, 426, 2797
- Wise, J. H., Turk, M. J., Norman, M. L., & Abel, T. 2012, ApJ, 745, 50
- Wolfe, A. M., Gawiser, E., & Prochaska, J. X. 2005, ARA&A, 43, 861
- Woosley, S. E., & Weaver, T. A. 1995, ApJS, 101, 181
- Worseck, G., et al. 2011, ApJ, 733, L24